

\*\*\*\*\*AUTO\*\*5-DIGIT 92103



#406387084# AS 07/26/13 6117  
MONTE MARSHALL  
235 QUINCE ST UNIT 402  
SAN DIEGO CA 92103-5847

P7  
642  
18

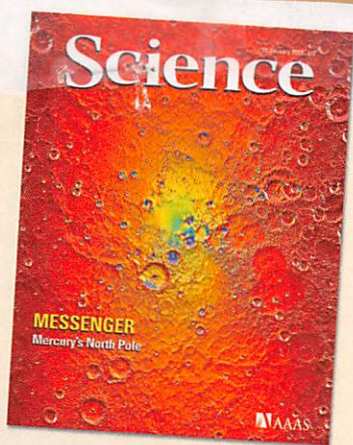
# MESSENGER

## Mercury's North Pole

# Science

18 January 2013 | \$10

MESSENGER, Mercury's North Pole  
M. 6417 | Dec 2012  
www.sciencemag.org

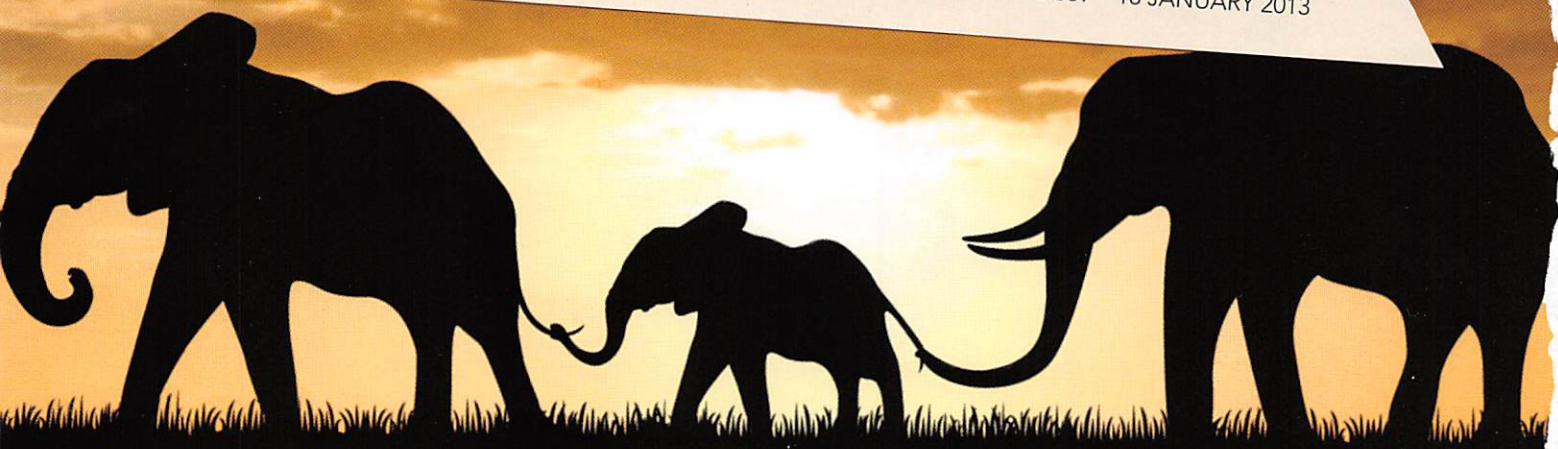


**COVER**

Map of highest surface temperature in the north polar region of Mercury superimposed on topography measured by the MESSENGER spacecraft. Red areas surrounding the pole (center) reach temperatures above 450 K. Blue and purple areas inside polar impact craters never exceed 100 K and are sufficiently cold to harbor water ice and frozen organic compounds. The largest ice-containing crater near the center of the image is ~112 km in diameter and 2.7 km deep. See pages 282, 292, 296, and 300. For the story behind the cover, go to <http://scim.ag/cov6117>.

Image: NASA/Johns Hopkins University Applied Physics Laboratory/Carnegie Institution of Washington/UCLA/David Paige

[www.sciencemag.org](http://www.sciencemag.org) **SCIENCE** VOL 339 18 JANUARY 2013



## Gibson Assembly™ Cloning Kit

New England Biolabs has revolutionized your laboratory's standard cloning methodology. The Gibson Assembly Cloning Kit combines the power of the Gibson Assembly Master Mix with NEB 5-alpha Competent *E. coli*, enabling fragment assembly and transformation in just under two hours. Save time, without sacrificing efficiency.

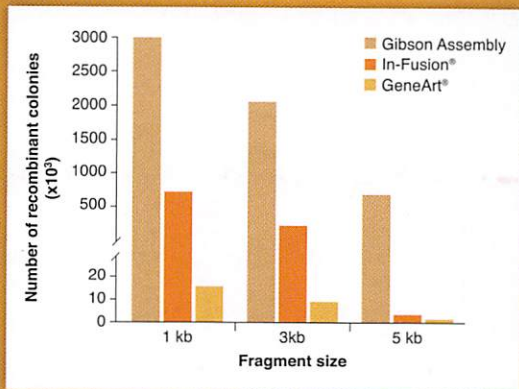
Making ends meet is now quicker and easier than ever before, with the Gibson Assembly Cloning Kit from NEB.

**NEBuilder™**  
 for Gibson Assembly

Visit [NEBGibson.com](http://NEBGibson.com) to view the latest tutorials and to try our primer design tool.

IN-FUSION® is a registered trademark of Clontech Laboratories, Inc.  
 GENEART™ is a registered trademark of Life Technologies, Inc.  
 GIBSON ASSEMBLY™ is a trademark of Synthetic Genomics, Inc.

Gibson Assembly Cloning Kit provides robust transformation efficiencies



Assembly reactions containing 25 ng of linear pUC19 vector and 0.04 pmol of each fragment were performed following individual suppliers' recommended protocols and using the competent cells provided with the kit. The total number of recombinant colonies was calculated per 25 ng of linear pUC19 vector added to the assembly reaction.

SYNTHETIC GENOMICS™

Some components of this product are manufactured by New England Biolabs, Inc. under license from Synthetic Genomics, Inc.

# Evidence for Water Ice Near Mercury's North Pole from MESSENGER Neutron Spectrometer Measurements

David J. Lawrence,<sup>1\*</sup> William C. Feldman,<sup>2</sup> John O. Goldsten,<sup>1</sup> Sylvestre Maurice,<sup>3</sup> Patrick N. Peplowski,<sup>1</sup> Brian J. Anderson,<sup>1</sup> David Bazell,<sup>1</sup> Ralph L. McNutt Jr.,<sup>1</sup> Larry R. Nittler,<sup>4</sup> Thomas H. Prettyman,<sup>2</sup> Douglas J. Rodgers,<sup>1</sup> Sean C. Solomon,<sup>4,5</sup> Shoshana Z. Weider<sup>4</sup>

Measurements by the Neutron Spectrometer on the Mercury Surface, Space ENvironment, GEochemistry, and Ranging (MESSENGER) spacecraft show decreases in the flux of epithermal and fast neutrons from Mercury's north polar region that are consistent with the presence of water ice in permanently shadowed regions. The neutron data indicate that Mercury's radar-bright polar deposits contain, on average, a hydrogen-rich layer more than tens of centimeters thick beneath a surficial layer 10 to 30 cm thick that is less rich in hydrogen. Combined neutron and radar data are best matched if the buried layer consists of nearly pure water ice. The upper layer contains less than 25 weight % water-equivalent hydrogen. The total mass of water at Mercury's poles is inferred to be  $2 \times 10^{16}$  to  $10^{18}$  grams and is consistent with delivery by comets or volatile-rich asteroids.

Earth-based measurements of radar-bright regions near Mercury's north and south poles were initially reported in 1992 (1), and subsequent measurements showed that these unusual radar characteristics are confined to per-

manently shadowed regions within high-latitude impact craters (2). The leading explanation for the high radar reflectance is the presence of large amounts of water ice that can be thermally stable in regions of permanent shadow over geologically long periods of time (2). One of the primary goals of NASA's Mercury Surface, Space ENvironment, GEochemistry, and Ranging (MESSENGER) mission is to characterize Mercury's polar regions and thereby identify the principal compositional component of the radar-bright regions. Here we report the results on hydrogen concentrations near Mercury's north pole from data acquired with MESSENGER's Neutron Spectrometer (NS).

Planetary neutron spectroscopy is a standard technique for remotely measuring planetary hydrogen concentrations (3). Neutrons are created by nuclear spallation reactions when high-energy cosmic rays strike the surface of an airless or nearly airless planetary body. The energy spectra of the resulting neutrons, which are typically created at energies ( $E_n$ ) exceeding ~1 to 10 MeV, are typically divided into three energy ranges: fast ( $E_n > 0.5$  MeV), epithermal ( $0.5 \text{ eV} < E_n < 0.5$  MeV), and thermal ( $E_n < 0.5$  eV) (Fig. 1A). Hydrogen has a unique ability to moderate neutrons because hydrogen atoms and neutrons have the same mass, which allows a highly efficient momentum transfer between the two. This efficient momentum transfer causes the number of epithermal neutrons to be strongly depressed so that they are highly sensitive to the presence of hydrogen in planetary materials. Fast neutrons are also sensitive to the presence of hydrogen but vary with hydrogen concentration by a factor of 2 less than epithermal neutrons (Fig. 1B). In addition, fast neutrons are sensitive to variations of average atomic mass ( $\langle A \rangle$ ) in dry planetary materials (4). Finally, fast and epithermal neutrons have different sensitivities to the depth and abundance of hydrogen within a hydrogen-rich layer that is covered by tens of centimeters of a hydrogen-poor material. Consequently, combined measurements of epithermal and fast neutrons have been used to determine the burial depth of a concentrated hydrogen layer (5).

The NS is a scintillator-based instrument that separately measures thermal, epithermal, and fast neutrons through a combination of spacecraft Doppler and coincidence pulse processing techniques (6). Because of its highly eccentric orbit, the MESSENGER spacecraft is at a moderately high altitude (200 to 600 km) when it passes over or near the radar-bright regions in Mercury's north

<sup>1</sup>The Johns Hopkins University Applied Physics Laboratory, Laurel, MD 20723, USA. <sup>2</sup>Planetary Science Institute, Tucson, AZ 85719, USA. <sup>3</sup>Institut de Recherche en Astrophysique et Planétologie, Université Paul Sabatier-CNRS-Observatoire Midi-Pyrénées, Toulouse, France. <sup>4</sup>Department of Terrestrial Magnetism, Carnegie Institution of Washington, Washington, DC 20015, USA. <sup>5</sup>Lamont-Doherty Earth Observatory, Columbia University, Palisades, NY 10964, USA.

\*To whom correspondence should be addressed. E-mail: david.j.lawrence@jhuapl.edu

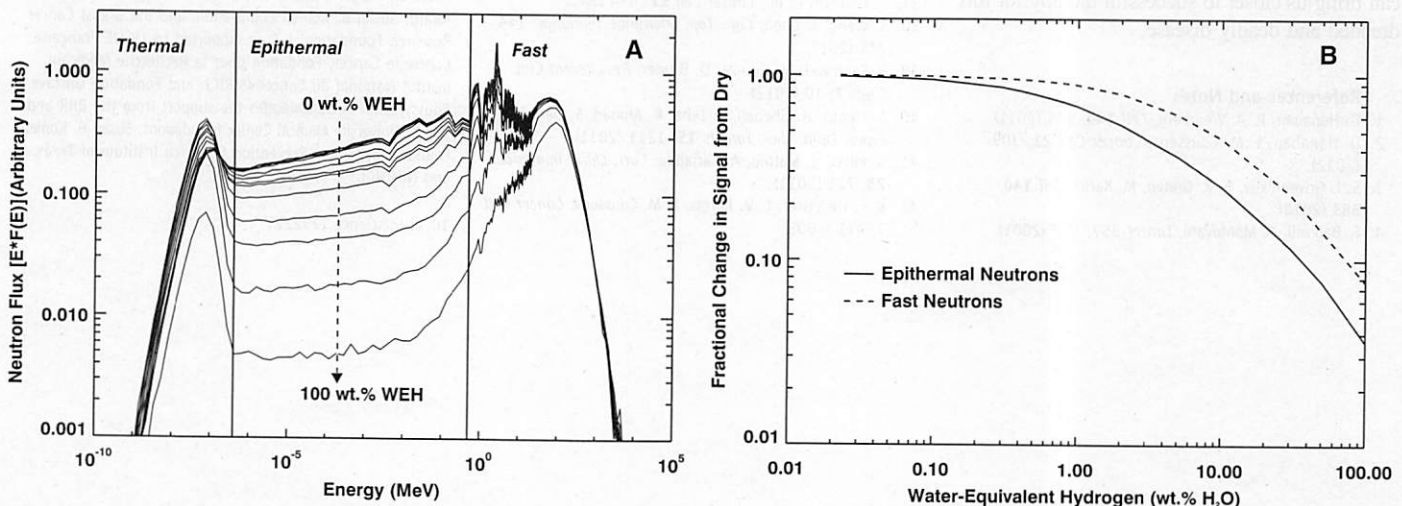


**Fig. 1.** (A) Simulated neutron flux, plotted as the product of energy and flux versus energy. Simulations were performed with the particle transport code MCNPX for a uniform sphere having Mercury's radius and appropriate soil composition (7, 9) but with a variable concentration of hydrogen from 0 wt %

water-equivalent hydrogen (WEH) to 100 wt % WEH. Nominal energy boundaries for thermal, epithermal, and fast neutrons are shown as vertical lines. (B) Simulated relative count rates on the MESSENGER NS for epithermal (solid) and fast (dashed) neutrons as a function of WEH for the same soil composition.

analogous to the improved survival now documented in metastatic melanoma patients treated with an antibody against the immunoregulatory molecule CTLA-4 (70) (e.g., ipilimumab), recently approved by the FDA. Given that PD-1 ligands are expressed in many tumor microenvironments, targeting the ligands, as opposed to their receptors, has the potential to be more effective and less toxic than current therapies targeting PD-1 and/or CTLA-4.

### Concluding Remarks

Inflammation represents a link between intrinsic (oncogenes, tumor suppressors, and genome stability genes) and extrinsic (immune and stromal components) factors contributing to tumor development. This knowledge offers new and novel candidate targets for therapeutic intervention, in combination with more conventional therapeutic approaches such as chemotherapy, radiotherapy, and targeted therapy. Therapeutic manipulation of chronic inflammation in tumors is likely to enhance the clinical efficacy of therapeutic vaccination as well as adoptive T cell transfer, thus turning the chronic pro-cancer inflammatory microenvironment into an anticancer microenvironment that is more likely to also liberate and activate existing anticancer effector T cells. Given the functional relevance of immune networking in tumors, it is imperative to incorporate immunometrics such as “the immunoscore” into traditional classification schemes to provide new prognostic and/or predictive tools to clinical practice (71, 72). A better identification of tissue- and/or tumor-specific inflammatory mechanisms (obtained through next-generation sequencing, metabolomics, and epigenetics) will allow us to direct the clinical management of cancer toward a more personalized medicine. A magic bullet? Yes, but not as stand-alone monotherapy. Rather, inflammation is another piece of the puzzle constituting hallmarks of cancer, the targeting of which can bring us closer to successful therapy for this dreaded and deadly disease.

### References and Notes

- D. Hanahan, R. A. Weinberg, *Cell* **144**, 646 (2011).
- D. Hanahan, L. M. Coussens, *Cancer Cell* **21**, 309 (2012).
- S. I. Grivennikov, F. R. Greten, M. Karin, *Cell* **140**, 883 (2010).
- F. Balkwill, A. Mantovani, *Lancet* **357**, 539 (2001).
- J. Bickels, Y. Kollender, O. Merinsky, I. Meller, *Isr. Med. Assoc. J.* **4**, 471 (2002).
- B. Ruffell, N. I. Afara, L. M. Coussens, *Trends Immunol.* **33**, 119 (2012).
- G. L. Beatty *et al.*, *Science* **331**, 1612 (2011).
- R. Wooster, K. E. Bachman, *Curr. Opin. Genet. Dev.* **20**, 336 (2010).
- A. Jemal, R. Siegel, J. Xu, E. Ward, *CA Cancer J. Clin.* **60**, 277 (2010).
- E. K. Wei, K. Y. Wolin, G. A. Colditz, *J. Clin. Oncol.* **28**, 4052 (2010).
- M. J. Thun, S. J. Henley, T. Gansler, *Novartis Found. Symp.* **256**, 6 (2004).
- F. Balkwill, K. A. Charles, A. Mantovani, *Cancer Cell* **7**, 211 (2005).
- L. M. Coussens, Z. Werb, *Nature* **420**, 860 (2002).
- A. Freund, A. V. Orjalo, P. Y. Desprez, J. Campisi, *Trends Mol. Med.* **16**, 238 (2010).
- T. D. Tlsty, L. M. Coussens, *Annu. Rev. Pathol.* **1**, 119 (2006).
- R. M. Steinman, J. Banchereau, *Nature* **449**, 419 (2007).
- P. Lu, K. Takai, V. M. Weaver, Z. Werb, *Cold Spring Harb. Perspect. Biol.* **3**, a005058 (2011).
- H. F. Dvorak, *N. Engl. J. Med.* **315**, 1650 (1986).
- J. A. Bluestone, C. R. Mackay, J. J. O’Shea, B. Stockinger, *Nat. Rev. Immunol.* **9**, 811 (2009).
- C. Tanchot *et al.*, *Cancer Microenviron.*, published online 27 October 2012 (10.1007/s12307-012-0122-y).
- A. H. Sharpe, E. J. Wherry, R. Ahmed, G. J. Freeman, *Nat. Immunol.* **8**, 239 (2007).
- H. Matsushita *et al.*, *Nature* **482**, 400 (2012).
- C. Dong, *Nat. Rev. Immunol.* **8**, 337 (2008).
- S. Wei, E. Zhao, I. Kryczek, W. Zou, *Oncoimmunology* **1**, 516 (2012).
- C. Aspord *et al.*, *J. Exp. Med.* **204**, 1037 (2007).
- Y. J. Liu *et al.*, *Annu. Rev. Immunol.* **25**, 193 (2007).
- A. Pedroza-Gonzalez *et al.*, *J. Exp. Med.* **208**, 479 (2011).
- V. Gocheva *et al.*, *Genes Dev.* **24**, 241 (2010).
- T. Shree *et al.*, *Genes Dev.* **25**, 2465 (2011).
- M. Terabe, J. M. Park, J. A. Berzofsky, *Cancer Immunol. Immunother.* **53**, 79 (2004).
- B. F. Skinnider, T. W. Mak, *Blood* **99**, 4283 (2002).
- W. J. Zhang *et al.*, *Cytokine* **42**, 39 (2008).
- V. N. Kristensen *et al.*, *Proc. Natl. Acad. Sci. U.S.A.* **109**, 2802 (2012).
- L. De Monte *et al.*, *J. Exp. Med.* **208**, 469 (2011).
- M. Kido *et al.*, *Infect. Immun.* **78**, 108 (2010).
- M. Di Piazza, C. S. Nowell, U. Koch, A. D. Durham, F. Radtke, *Cancer Cell* **22**, 479 (2012).
- S. Demehri *et al.*, *Cancer Cell* **22**, 494 (2012).
- S. Wang, L. Chen, *Curr. Top. Microbiol. Immunol.* **344**, 245 (2011).
- P. Sakhivel, M. Gereke, D. Bruder, *Rev. Recent Clin. Trials* **7**, 10 (2012).
- A. Hasan, H. Ghebeh, C. Lehe, R. Ahmad, S. Dermime, *Expert Opin. Ther. Targets* **15**, 1211 (2011).
- S. Pillai, H. Mattoo, A. Cariappa, *Curr. Opin. Immunol.* **23**, 721 (2011).
- K. E. de Visser, L. V. Korets, L. M. Coussens, *Cancer Cell* **7**, 411 (2005).
- P. Andreu *et al.*, *Cancer Cell* **17**, 121 (2010).
- T. Schioppa *et al.*, *Proc. Natl. Acad. Sci. U.S.A.* **108**, 10662 (2011).
- K. M. Haas, J. C. Poe, D. A. Steeber, T. F. Tedder, *Immunity* **23**, 7 (2005).
- M. Horikawa, V. Minard-Colin, T. Matsushita, T. F. Tedder, *J. Clin. Invest.* **121**, 4268 (2011).
- Y. Sun *et al.*, *Nat. Med.* **18**, 1359 (2012).
- M. Ammirante, J. L. Luo, S. Grivennikov, S. Nedospasov, M. Karin, *Nature* **464**, 302 (2010).
- D. G. DeNardo *et al.*, *Cancer Cell* **16**, 91 (2009).
- C. A. Dinarello, *Cancer Metastasis Rev.* **29**, 317 (2010).
- F. R. Balkwill, A. Mantovani, *Semin. Cancer Biol.* **22**, 33 (2012).
- M. S. Anglesio *et al.*, *Clin. Cancer Res.* **17**, 2538 (2011).
- P. Geborek *et al.*, *Ann. Rheum. Dis.* **64**, 699 (2005).
- T. Bongartz *et al.*, *JAMA* **295**, 2275 (2006).
- B. Z. Qian *et al.*, *Nature* **475**, 222 (2011).
- D. Z. Qian *et al.*, *Prostate* **70**, 433 (2010).
- S. V. Kozin *et al.*, *Cancer Res.* **70**, 5679 (2010).
- A. F. Welford *et al.*, *J. Clin. Invest.* **121**, 1969 (2011).
- D. G. DeNardo *et al.*, *Cancer Discov.* **1**, 54 (2011).
- A. H. Beck *et al.*, *Clin. Cancer Res.* **15**, 778 (2009).
- M. J. Campbell *et al.*, *Breast Cancer Res. Treat.* **128**, 703 (2011).
- Y. Pylayeva-Gupta, K. E. Lee, C. H. Hajdu, G. Miller, D. Bar-Sagi, *Cancer Cell* **21**, 836 (2012).
- L. J. Bayne *et al.*, *Cancer Cell* **21**, 822 (2012).
- A. Kessel, I. Rosner, E. Toubi, *Clin. Rev. Allergy Immunol.* **34**, 74 (2008).
- T. T. Tan, L. M. Coussens, *Curr. Opin. Immunol.* **19**, 209 (2007).
- B. Zbar, T. Tanaka, *Science* **172**, 271 (1971).
- S. Adams *et al.*, *Clin. Cancer Res.* **18**, 6748 (2012).
- G. Heber *et al.*, *J. Dtsch. Dermatol. Ges.* **7**, 534 (2009).
- J. R. Brahmer *et al.*, *J. Clin. Oncol.* **28**, 3167 (2010).
- F. S. Hodi *et al.*, *N. Engl. J. Med.* **363**, 711 (2010).
- J. Galon *et al.*, *J. Transl. Med.* **10**, 205 (2012).
- J. Galon *et al.*, *J. Transl. Med.* **10**, 1 (2012).
- A. L. Doedens *et al.*, *Cancer Res.* **70**, 7465 (2010).

**Acknowledgments:** The authors thank members of their laboratories for critical discussions on content and specifically A. Gunderson and B. Ruffell for critical reading of the manuscript. L.M.C. acknowledges support from the NIH/National Cancer Institute (NCI), a Department of Defense Breast Cancer Research Program Era of Hope Scholar Scholar Expansion Award, Susan B. Komen Foundation, and the Breast Cancer Research Foundation. L.Z. is supported by LIGUE Française Contre le Cancer, Fondation pour la Recherche Médicale, Institut National du Cancer (SIRIC), and Fondation Gustave Roussy. A.K.P. acknowledges the support from the BIIR and Baylor University Medical Center foundations, Susan B. Komen Foundation, Cancer Prevention Research Institute of Texas, and NIH/NCI.

10.1126/science.1232227

polar region. As a consequence, the omnidirectional neutron measurements have a large spatial footprint (300 to 900 km full-width, half maximum) compared with the size of the radar-bright regions (<40 km), so individual deposits cannot be spatially resolved (7). If extensive water ice is present in the locations of the radar-bright regions, fast and epithermal neutron count rates will show a count rate decrease of 4% or less poleward of latitudes 60° to 70° compared with count rates at lower latitudes (7).

NS data analysis has been carried out with empirically derived corrections applied in parallel with a neutron count rate simulation (8). The count rate simulation, which was validated with flyby data (9), accounts for the near-surface production of neutrons by galactic cosmic rays, their transport to the spacecraft, and their detection by the NS. The simulation was used to guide and constrain the empirical corrections and to provide a capability for bounding the surface hydrogen concentrations. The NS analysis requires corrections to account for nonisotropic solid angle variations, spacecraft obscuration effects, time variations in the incident cosmic ray flux, near-surface temperature variations, and variations from a radial velocity Doppler effect. The radial Doppler effect arises because the speed of the MESSENGER spacecraft in the direction of the spacecraft–planet-center vector has a magnitude (0 to 2 km/s) that is similar to the speed of thermal and low-energy epithermal neutrons (~2 km/s) (10). Doppler-induced effects are negligible for fast neutrons but have a magnitude of a few percent for low-energy epithermal neutrons and therefore need to be considered.

Fully corrected, longitudinally averaged count rates for fast neutrons are shown in Fig. 2 as a function of latitude for data collected from 26 March 2011 to 25 February 2012 (8). Simulated count rates were calculated for the measured count rate collection periods and include all viewing geometry effects. The simulation shows that if the radar-bright regions contain no hydrogen, fast neutrons would display no latitude dependence. In contrast, when a thick surface layer (i.e., having a thickness greater than the depth of sensitivity of the NS) consisting of 100 weight % (wt %) water-equivalent hydrogen (WEH) is included within all mapped radar-bright regions, the simulation shows a poleward decrease of 1.8% in fast neutrons relative to count rates closer to the equator. The NS measurements, in comparison, show a poleward decrease of 1.1% (Fig. 2) (8). When the latitude-dependent signal is averaged over two latitude zones (northward of 75°N and southward of 45°N), the fast neutron count rate at the north pole has a value of  $0.9898 \pm 0.0020$  (two standard deviations, or  $2\sigma$ ) relative to unity at the equator with a statistical significance of  $11\sigma$  (8). In comparison, simulated count rates with comparable Poisson uncertainties show that if the radar-bright regions were to contain a thick surface layer of 100 wt % water ice, then there would be a  $0.978 \pm 0.001$  ( $2\sigma$ ) signal with an  $18\sigma$  statistical significance (8).

To interpret the fast neutron data, variations in the fast neutron flux unrelated to hydrogen must first be understood. From surface elemental abundances on Mercury (11–15) and assumptions on probable mineralogical assemblages (8), the value of  $\langle A \rangle$  for Mercury's northern volcanic plains (16) may be lower by as much as 0.06 to 0.18 atomic mass unit (amu) than for the surrounding intercrater plains and heavily cratered terrain (8). With the longitudinally averaged data, an  $\langle A \rangle$  decrease in the northern plains is likely to be indistinguishable from a hydrogen signal from radar-bright areas given the broad spatial footprint and limited statistics of the fast neutron data. A 0.06 to 0.18 amu change in  $\langle A \rangle$  corresponds to a 0.6 to 1.8% decrease in relative fast neutron count rate (4). In principle,  $\langle A \rangle$  variations could account for some or all of the fast neutron signal, so that signal is  $0.9898 (-0.0020, +0.0102)$  (8) when all uncertainties are combined.

Two conclusions follow from the polar measurements of fast neutrons. First, the measured polar decrease is a factor of 2 smaller than expected if all radar-bright regions contained pure or nearly pure (80 to 100 wt %) water ice at the surface, so these data do not support the presence of thick surficial deposits of water ice in all radar-bright regions. Second, the regional dynamic range of ~1% for fast neutrons on Mercury is substantially smaller than that measured for Vesta (~10%) (17), the Moon (~38%) (18), or Mars (~300%) (19), where variations in  $\langle A \rangle$  and/or hydrogen dominate. A 1% fast neutron dynamic range therefore places strong constraints on the major-element variability across Mercury's surface on the spatial scale (few hundreds to 1000 km) of the NS footprints.

Fully corrected, longitudinally averaged count rates for epithermal neutrons are shown as a function of latitude in Fig. 3 (8). Data collection times and selections for epithermal neutrons are the same as those for fast neutrons. The monotonic equator-to-pole variation is due mostly to the radial Doppler effect, which is treated in the latitudinally binned count rates by normalizing both the 100 wt % WEH simulation results and the measurements to the no-water simulation rates (Fig. 3B).

The dominant, remaining signal in the measured epithermal neutron data is a decrease at high latitudes, relative to the no-water simulation, that starts near latitude 70°N. The magnitude and latitude profile of this variation closely matches that of the simulated count rate for a thick, surficial layer of 100 wt % water ice at all the radar-bright regions identified from radar observations (2). The good agreement between the data and simulation provides strong evidence that large amounts of hydrogen in the form of water ice are present in Mercury's radar-bright regions. Using the highest-latitude value as the maximum polar signal, the epithermal neutron data show a measured polar signal of  $0.976 \pm 0.0025$  ( $2\sigma$ ), relative to an equatorial neutron signal of 1. Despite this strong polar signal, relating the magnitude of the polar decrease of epithermal neutrons to a hydrogen concentration within the radar-bright regions requires careful consideration of other sources of variability within the epithermal neutron data.

Differences between data and simulations that are unrelated to the high-latitude signal have magnitudes of ~0.2 to 0.5% (Fig. 3A), which are at least a factor of 5 smaller than the measured

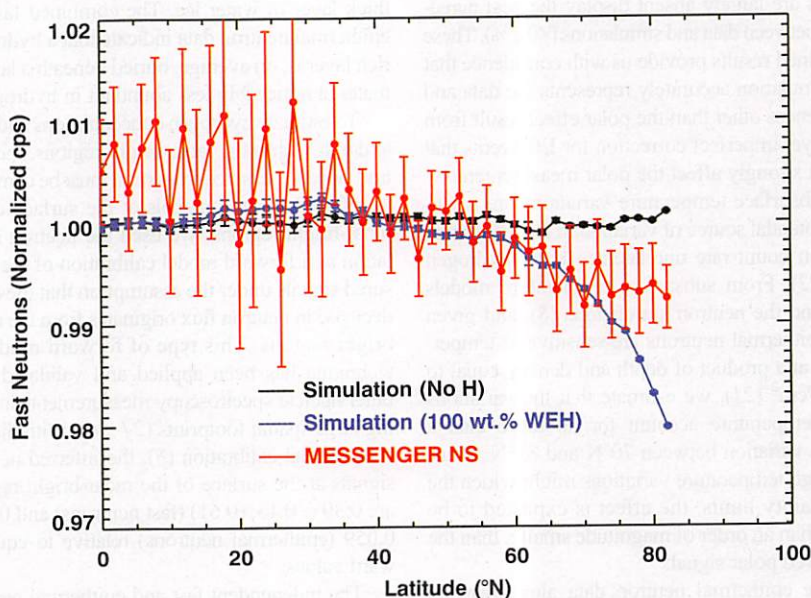


**Fig. 2.** Measured (red) and simulated (black, blue) fast neutron count rates in units of normalized counts per second (cps) averaged over 2°-wide latitude bins and plotted as a function of latitude. All corrections (8) have been applied. Counts are normalized to the mean count rate (~10 cps) at an altitude of 400 km. Simulated count rates are shown for the cases of no hydrogen (black) and for a thick layer of 100 wt % water ice (blue) located at the surface in all radar-bright regions. The error bars denote twice the measured standard deviation of the mean in each latitude bin.

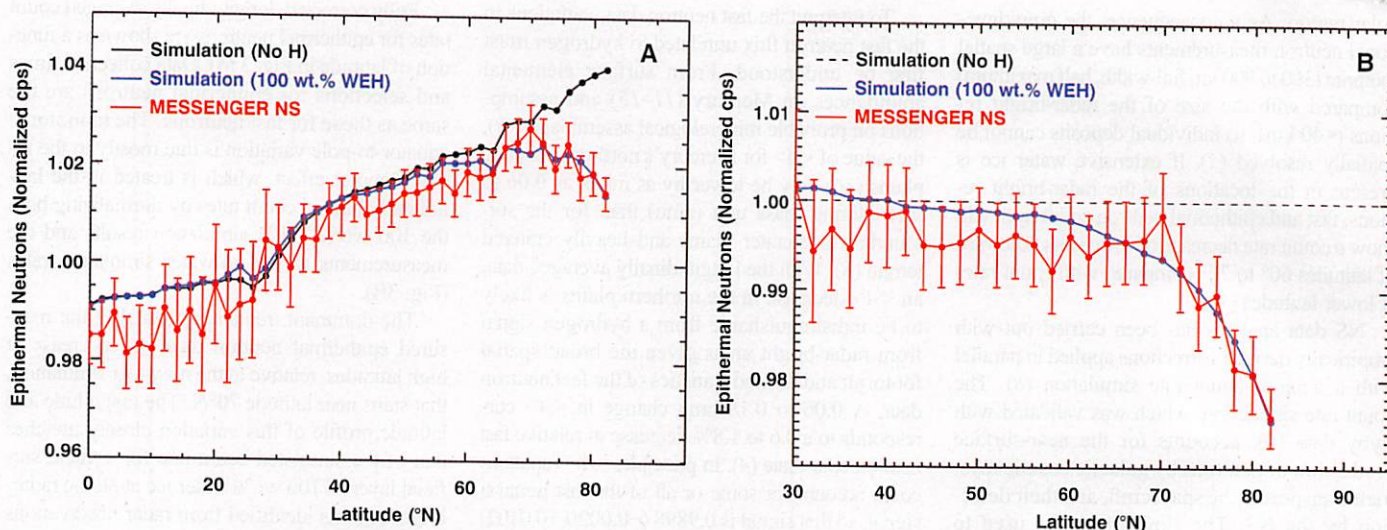


**Fig. 3.** (A) Measured (red) and simulated (black, blue) epithermal neutron count rates averaged over 2°-wide latitude bins and plotted as a function of latitude. All corrections except for a radial Doppler effect have been applied to the data ( $\beta$ ). Counts are normalized to the mean count rate (~60 cps) at an altitude of 400 km. Simulated count rates are shown for the cases of no

hydrogen (black) and a thick surficial layer of 100% water ice (blue) in all radar-bright regions. The error bars denote twice the measured standard deviation of the mean in each latitude bin. (B) Simulated and measured epithermal neutron count rates after correcting for the radial Doppler effect, which is accomplished by normalizing to the simulation with no hydrogen.

latitudinal signal of 2.4%. These differences are most notable at latitudes of 0° to 20°N and 40° to 60°N. These are latitude ranges over which the spacecraft is known to interact with populations of energetic electrons (EEs) on nearly every orbit (20). The presence of small EE events results in a systematic underestimate of the net neutron counts (8). An empirical correction was applied to reduce the magnitude of this effect to give the 0.2 to 0.5% level seen in Fig. 3A. Nonpolar latitude ranges (30° to 40°N and >60°N) over which EE events are largely absent display the best agreement between data and simulations (<0.2%). These combined results provide us with confidence that the simulation accurately represents the data and differences other than the polar effect result from an as yet imperfect correction for EE events that do not strongly affect the polar measurement.

Subsurface temperature variations are a second potential source of variation in the epithermal neutron count rate unrelated to polar hydrogen (21, 22). From subsurface temperature models (23) and the neutron simulations (8), and given that epithermal neutrons are sensitive to temperatures at a product of depth and density equal to ~30 g/cm<sup>2</sup> (21), we estimate that the variations with temperature account for no more than a 0.16% variation between 70°N and 85°N. Thus, although temperature variations might widen the uncertainty limits, the effect is expected to be more than an order of magnitude smaller than the measured polar signal.

The epithermal neutron data alone provide strong evidence that Mercury's north polar radar-bright regions contain high concentrations of hydrogen, consistent with the presence of water ice. If it is assumed that the water ice is located within the radar-bright regions as a single thick layer, then the epithermal neutron data are consistent

with the presence of up to 100 wt % WEH within these regions. That the 2 $\sigma$  uncertainty of the measurements extends to a slightly larger signal than is given for the hydrogen-rich simulation indicates that the epithermal neutron data are consistent with (but do not require) a larger total area than is specified by the known radar-bright regions. In either case, however, the inferred hydrogen concentration with a single-layer assumption is not consistent with the fast neutron data, which exhibit a smaller signal than expected for a single thick layer of water ice. The combined fast and epithermal neutron data indicate that a hydrogen-rich layer is, on average, buried beneath a layer of material noticeably less abundant in hydrogen.

To estimate hydrogen concentrations and burial depth within the radar-bright regions, the neutron signals measured from orbit must be converted to inferred neutron signals at the surface of the radar-bright regions. We used the neutron simulation as a forward model calibration of the measured signals under the assumption that the entire decrease in neutron flux originates from the radar-bright regions. This type of forward modeling technique has been applied and validated with other nuclear spectroscopy measurements involving large spatial footprints (24–26). With the forward model calibration (8), the inferred neutron signals at the surface of the radar-bright regions are 0.39 (–0.13,+0.61) (fast neutrons) and 0.10  $\pm$  0.059 (epithermal neutrons) relative to equatorward values.

The independent fast and epithermal neutron measurements allow us to use a two-layer model with two free parameters constrained by the measurements (average thickness of the upper layer and hydrogen concentration in one of the layers). We considered two end-member models. For model 1, we assumed that the upper layer contains no

hydrogen ( $w_{\text{upper}} = 0$  wt % WEH), so that the effective thickness ( $t$ ) of the upper layer, expressed as the product of density and thickness, and the hydrogen content of the lower layer ( $w_{\text{lower}}$ ) are constrained by the data. For model 2, we assumed that the lower layer has  $w_{\text{lower}} = 100$  wt % WEH, so that the effective thickness and hydrogen concentration of the upper layer are constrained by the data. These layering models represent an average layering structure, and actual layering need not correspond to a uniform two-layer stratigraphy across the NS field of view for all radar-bright regions. A distribution of different layer configurations among or within radar-bright regions can also satisfy the current data.

From modeled neutron fluxes convolved with the respective NS efficiencies, we calculated the relative count rates for fast and epithermal neutrons for a range of hydrogen concentrations and upper-layer thicknesses in the two-layer models. For model 1 (Fig. 4A),  $t = 12$  to 47 g/cm<sup>2</sup> and  $w_{\text{lower}} = 12$  to 100 wt % WEH. For model 2 (Fig. 4B),  $t = 12$  to 47 g/cm<sup>2</sup> and  $w_{\text{upper}} = 0$  to 25 wt % WEH. These results are consistent with an average two-layer stratigraphy in which the hydrogen concentration in the upper layer is 0 to 25 wt % WEH, the hydrogen concentration in the lower layer is 12 to 100 wt % WEH, and the effective thickness of the upper layer is 12 to 47 g/cm<sup>2</sup>. If a typical planetary regolith density of 1.5 g/cm<sup>3</sup> is assumed (27), this effective thickness corresponds to a physical thickness of 8 to 31 cm.

Although we have analyzed the NS data in the context of large hydrogen concentrations within Mercury's permanently shadowed regions, other physical distributions of hydrogen can be considered. One possible distribution is a broad area of hydrogen enrichment poleward of ~70°N in which the hydrogen is emplaced in a single

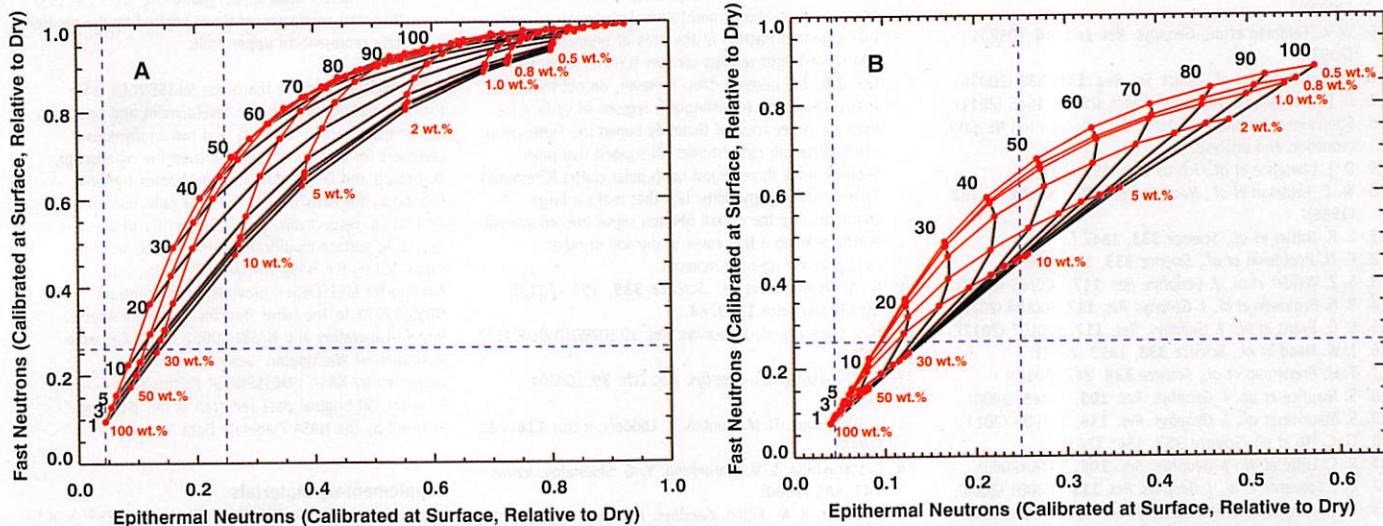


**Fig. 4.** (A) Simulated epithermal versus fast neutron relative count rates at the surface of the radar-bright regions for a two-layer model stratigraphy (model 1) with a range of values for the thickness of the upper layers and the hydrogen concentration of the lower layer. Black lines and numbers indicate upper-layer thickness contours in units of  $\text{g}/\text{cm}^2$ . Red lines and numbers indicate contours of lower-layer hydrogen concentrations in units of WEH wt %. Vertical dashed blue

lines show the  $2\sigma$  limits of the calibrated epithermal neutron measurements; the horizontal dashed blue line shows the lower  $2\sigma$  limit of the fast neutron measurement. The lower and upper thickness values are constrained by the fast and epithermal neutrons, respectively. (B) Simulated and measured fast and epithermal neutron count rates for model 2; hydrogen concentration values are shown for an upper layer over a thick layer of 100 wt % water ice.

layer by solar wind. For this scenario, the measured epithermal neutron signal of 2.4% fills the NS field of view, and an average hydrogen concentration can be determined (28) to be 50 parts per million (ppm). The fast neutrons provide few constraints, as the measurement uncertainties allow a hydrogen concentration of 0 to 100 ppm (28). Nevertheless, given the excellent agreement of the epithermal neutron data with the simulation (Fig. 3) along with the strong consistency of the neutron data with other data sets, we consider that the NS observations are better understood as the result of enhanced concentrations of water ice within the radar-bright regions.

The NS results are consistent with observations made by the MESSENGER Mercury Laser Altimeter (MLA) and the Mercury Dual Imaging System (MDIS). Topographic data from MLA, together with thermal models derived from the topography, have shown that for the majority of the north polar radar-bright regions sampled by MLA, water ice is not stable at the surface (23, 29). These studies suggest that any thick water ice layer in these areas is located beneath an insulating layer  $\sim 10$  cm thick, and MLA reflectance measurements indicate that this surficial layer is darker than surrounding terrain at 1064-nm wavelength and may be enriched in hydrocarbon materials (30). The NS results, which indicate that the upper of the two layers in the north polar deposits has no more than 25 wt % WEH, are consistent with the interpretation that the radar-bright regions contain complex hydrocarbons, possibly mixed with silicate regolith. Images of the north and south polar regions by MDIS (31, 32) have revealed a nearly one-to-one correspondence between radar-bright regions and areas of permanent or at least persistent shadow. Because the

neutron simulations used the same locations of radar-bright features as the illumination studies, the combined results provide a self-consistent basis for interpreting the locations of hydrogen, permanent shade, and radar-bright deposits.

With the identification from neutron spectrometry of large concentrations of hydrogen within the radar-bright regions, it may now be concluded that the high radar backscatter of the polar deposits is the result of nearly pure water ice (2). This consideration favors our model 2, with an assumed hydrogen concentration in the lower layer of  $w_{\text{lower}} = 100$  wt % WEH. Multi-wavelength radar data also support the interpretation that the water-rich layer, on average, is buried beneath an insulating layer of  $\sim 10$ -cm thickness (2). This thickness falls within the range of 8 to 31 cm inferred from the neutron data. The identification of large hydrogen concentrations within the radar-bright regions makes unnecessary such alternative explanations for the high radar backscatter as enhanced concentrations of sulfur (33) or unusual radar properties of silicate materials at low temperatures (34).

Given that the water ice in the polar deposits must be nearly pure, models of surface modification processes (burial and excavation by impacts, loss from ion sputtering and other surface processes, and addition of material from the atmosphere and micrometeoroids) in Mercury's polar region have shown that the bottom layer of deposits must be at least tens of centimeters thick (35). If we use a maximum lower-layer thickness of tens of meters as estimated from models of radar scattering (36) and an estimate of the area of permanent shadow in the north polar region of  $(1.25 \text{ to } 1.46) \times 10^{14} \text{ cm}^2$  (2), then an estimate of the total mass of water in the north polar region

may be calculated. For a lower-layer thickness in the range 0.5 to 20 m, the total mass of water ranges from  $6.2 \times 10^{15} \text{ g}$  to  $2.9 \times 10^{17} \text{ g}$ . If we assume that the radar-reflective regions in the south polar region are also dominantly water ice, then from the area of permanently shadowed regions at high southern latitudes of  $(4.3 \pm 1.4) \times 10^{14} \text{ cm}^2$  (32), the total mass of ice in the south polar area ranges from  $1.5 \times 10^{16}$  to  $1.1 \times 10^{18} \text{ g}$ , and the total mass of ice in both polar regions is  $2.1 \times 10^{16}$  to  $1.4 \times 10^{18} \text{ g}$ . The total mass could be larger if the lower-layer thickness is greater than 20 m. The mass inferred here is consistent with values estimated earlier (37), and the delivery of this amount of water is possible from the impact of some combination of comets and volatile-rich asteroids onto Mercury (37) followed by migration to the poles with a polar cold-trapping rate of 5 to 15% (38). Models of surface modification that account for vertical and lateral mixing averaged over large areas indicate that a pure water ice deposit will be buried by drier material at a rate of 0.43 cm per million years (My) (35, 39). The average thickness of the upper layer inferred from neutron spectrometry therefore suggests that Mercury's polar water ice was emplaced sometime in the last 18 to 70 My.

*Note added in proof:* Text has been modified from the version published in *Science Express* (8).

#### References and Notes

1. M. A. Slade, B. J. Butler, D. O. Muhleman, *Science* **258**, 635 (1992).
2. J. K. Harmon, M. A. Slade, M. S. Rice, *Icarus* **211**, 37 (2011).
3. T. H. Prettyman, Remote chemical sensing using nuclear spectroscopy, in *Encyclopedia of the Solar System*, L. A. McFadden, P. R. Weissman, T. V. Johnson, Eds. (Academic Press, San Diego, CA, ed. 2, 2007), pp. 765–786.

4. O. Gasnault *et al.*, *Geophys. Res. Lett.* **28**, 3797 (2001).
5. W. C. Feldman *et al.*, *Geophys. Res. Lett.* **34**, L05201 (2007).
6. J. O. Goldsten *et al.*, *Space Sci. Rev.* **131**, 339 (2007).
7. D. J. Lawrence *et al.*, *Planet. Space Sci.* **59**, 1665 (2011).
8. Supplementary online material describes the full NS data reduction and analysis.
9. D. J. Lawrence *et al.*, *Icarus* **209**, 195 (2010).
10. W. C. Feldman *et al.*, *Nucl. Instrum. Methods A* **245**, 182 (1986).
11. L. R. Nittler *et al.*, *Science* **333**, 1847 (2011).
12. P. N. Peplowski *et al.*, *Science* **333**, 1850 (2011).
13. S. Z. Weider *et al.*, *J. Geophys. Res.* **117**, E00L05 (2012).
14. P. N. Peplowski *et al.*, *J. Geophys. Res.* **117**, E00L04 (2012).
15. L. G. Evans *et al.*, *J. Geophys. Res.* **117**, E00L07 (2012).
16. J. W. Head *et al.*, *Science* **333**, 1853 (2011).
17. T. H. Prettyman *et al.*, *Science* **338**, 242 (2012).
18. S. Maurice *et al.*, *J. Geophys. Res.* **105**, 20365 (2000).
19. S. Maurice *et al.*, *J. Geophys. Res.* **116**, E11008 (2011).
20. G. C. Ho *et al.*, *Science* **333**, 1865 (2011).
21. R. C. Little *et al.*, *J. Geophys. Res.* **108**, 5046 (2003).
22. D. J. Lawrence *et al.*, *J. Geophys. Res.* **111**, E08001 (2006).
23. D. A. Paige *et al.*, *Science* **339**, 300 (2013); 10.1126/science.1231106.
24. D. J. Lawrence *et al.*, *Geophys. Res. Lett.* **32**, L07201 (2005).
25. J. J. Hagerty *et al.*, *J. Geophys. Res.* **111**, E06002 (2006).
26. T. D. Glotch *et al.*, *Geophys. Res. Lett.* **38**, L21204 (2011).
27. W. D. Carrier III, G. R. Olhoeft, W. Mendell, in *Lunar Sourcebook: A User's Guide to the Moon*, G. Heiken, D. Vaniman, B. M. French, Eds. (Cambridge Univ. Press, 1991), pp. 475–594.
28. W. C. Feldman *et al.*, *Science* **281**, 1496 (1998).
29. There is observational and thermal modeling evidence that a limited fraction of the area of permanent shadow and radar-bright regions contain surficial water ice (23, 30). The neutron data, however, do not have the spatial resolution to distinguish regions of surface ice from the larger areas of shallowly buried ice. Furthermore, multiwavelength radar studies (2) suggest that polar deposits in the three largest north polar craters [Chesterton, Tolkien, and Tryggvadóttir (2)] that make a large contribution to the overall neutron signal are, on average, buried beneath a thin cover of dry soil or other comparatively ice-poor material.
30. G. A. Neumann *et al.*, *Science* **339**, 296 (2013); 10.1126/science.1229764.
31. N. L. Chabot *et al.*, *J. Geophys. Res.* **10.1029/2012JE004172** (2012).
32. N. L. Chabot *et al.*, *Geophys. Res. Lett.* **39**, L09204 (2012).
33. A. L. Sprague, D. M. Hunten, K. Lodders, *Icarus* **118**, 211 (1995).
34. L. Starukhina, L. V. Starukhina, Y. G. Shkuratov, *Icarus* **147**, 585 (2000).
35. D. Crider, R. M. Killen, *Geophys. Res. Lett.* **32**, L12201 (2005).
36. B. J. Butler, D. O. Muhleman, M. A. Slade, *J. Geophys. Res.* **98**, 15003 (1993).
37. J. I. Moses, K. Rawlins, K. Zahnle, L. Dones, *Icarus* **137**, 197 (1999).
38. B. J. Butler, *J. Geophys. Res.* **102**, 19283 (1997).
39. The surface modification models do not account for thermal effects (23) that can operate on time scales much shorter than impact gardening processes (35). Thus, the emplacement times implied by the neutron data represent an upper limit.

**Acknowledgments:** We thank the MESSENGER team for their contributions to the development and operation of the spacecraft, P. G. Lucey and two anonymous reviewers for comments that improved the manuscript, D. Delapp and D. Seagraves of Los Alamos National Laboratory for early help in the data reduction and calibration, respectively, and D. Hurley for discussions regarding surface modification models. This work was supported by the NASA Discovery Program, with funding for MESSENGER provided under contract NAS5-97271 to The Johns Hopkins University Applied Physics Laboratory and NASW-00002 to the Carnegie Institution of Washington. Several authors are supported by NASA's MESSENGER Participating Scientist Program. All original data reported in this paper are archived by the NASA Planetary Data System.

**Supplementary Materials**  
www.sciencemag.org/cgi/content/full/science.1229953/DC1  
Supplementary Text  
Figs. S1 to S23  
Tables S1 to S4  
References (40–51)

10 September 2012; accepted 13 November 2012  
Published online 29 November 2012;  
10.1126/science.1229953

## Bright and Dark Polar Deposits on Mercury: Evidence for Surface Volatiles

Gregory A. Neumann,<sup>1\*</sup> John F. Cavanaugh,<sup>1</sup> Xiaoli Sun,<sup>1</sup> Erwan M. Mazarico,<sup>2</sup> David E. Smith,<sup>2</sup> Maria T. Zuber,<sup>2</sup> Dandan Mao,<sup>3</sup> David A. Paige,<sup>4</sup> Sean C. Solomon,<sup>5,6</sup> Carolyn M. Ernst,<sup>7</sup> Olivier S. Barnouin<sup>7</sup>

Measurements of surface reflectance of permanently shadowed areas near Mercury's north pole reveal regions of anomalously dark and bright deposits at 1064-nanometer wavelength. These reflectance anomalies are concentrated on poleward-facing slopes and are spatially collocated with areas of high radar backscatter postulated to be the result of near-surface water ice. Correlation of observed reflectance with modeled temperatures indicates that the optically bright regions are consistent with surface water ice, whereas dark regions are consistent with a surface layer of complex organic material that likely overlies buried ice and provides thermal insulation. Impacts of comets or volatile-rich asteroids could have provided both dark and bright deposits.

Mercury's near-zero obliquity and impact-roughened topography (1) prevent direct sunlight from reaching substantial portions of its polar regions. Lacking major con-

vective or conductive sources of heat, the permanently shadowed, near-surface regolith experiences temperatures similar to those of the icy Galilean satellites (2). It has long been believed on theoretical grounds that such conditions are favorable to the accumulation of volatiles (3, 4). Even with Mercury's close proximity to the Sun, extremes of daytime temperature are not expected to penetrate regolith to substantial depth, allowing near-surface water ice, if present, to remain stable against sublimation for billions of years (2). Such hypotheses were renewed when Earth-based radar observations of Mercury, at wavelengths from 3.6 to 70 cm (5–9), revealed regions of high backscatter and depolarization at both poles. Radar observations suggested that depo-

sits of nearly pure water ice up to several meters thick lie at or near the surface. Analysis of altimetry and roughness measurements from the Mercury Laser Altimeter (MLA) (10, 11) on the MErcury Surface, Space ENvironment, GEochemistry, and Ranging (MESSENGER) spacecraft (12) indicates that craters hosting radar-bright deposits at high northern latitudes are not anomalously shallow, nor do they display distinctive roughness properties in comparison with craters that lack such deposits (13). Consequently, the radar-bright material does not form a thick layer overlying regolith (13). A thinner surficial layer containing substantial concentrations of ice would, however, be optically brighter than the surrounding terrain (14) and should be detectable by active remote sensing.

We report here measurements with MLA of surface reflectance in permanently shadowed north polar regions of Mercury. The MLA instrument illuminates surface spots 20 to 80 m in diameter at 350- to 450-m intervals (10). The receiver system measures threshold-crossing times of the received pulse waveforms at two voltages (15). A single low-threshold crossing provides surface elevation, and the timing of the rising and falling signal levels for strong returns at both low and high thresholds enables MLA to estimate the received pulse energy and make active measurements of surface reflectance,  $r_s$ , via the lidar link equation (16, 17) and preflight sensor calibrations (10).

During its primary mapping mission, MESSENGER orbited Mercury in an eccentric orbit with a 12-hour period and a ~200- to 400-km periapsis altitude at 60° to 70°N. In this orbit, the MLA ranged to Mercury from 29 March 2011

<sup>1</sup>NASA Goddard Space Flight Center, Code 698, Greenbelt, MD 20771, USA. <sup>2</sup>Department of Earth, Atmospheric, and Planetary Sciences, Massachusetts Institute of Technology, Cambridge, MA 02139, USA. <sup>3</sup>Sigma Space Corporation, Lanham, MD 20706, USA. <sup>4</sup>Department of Earth and Space Sciences, University of California, Los Angeles, CA 90095, USA. <sup>5</sup>Department of Terrestrial Magnetism, Carnegie Institution of Washington, Washington, DC 20015, USA. <sup>6</sup>Lamont-Doherty Earth Observatory, Columbia University, Palisades, NY 10964, USA. <sup>7</sup>The Johns Hopkins Applied Physics Laboratory, Laurel, MD 20723, USA.

\*To whom correspondence should be addressed. E-mail: gregory.a.neumann@nasa.gov



to 16 April 2012, densely sampling the north polar region in nadir mode northward to 83.5°N and sparsely in off-nadir mode at more northerly latitudes (Fig. 1A) (1). More than 4 million topographic and 2 million reflectance measurements were collected at latitudes greater than 65°N in the first year of mapping. Of 700 orbital profiles, 60 targeted latitudes higher than 84°N with off-nadir ranges, some yielding energy measurements and some not (fig. S1). Orbital geometry and power and thermal constraints precluded observations of many polar craters, and measurements of those that were accessible at oblique incidence returned noisier measurements than at nadir orientation.

A map of radar cross section in the north polar region at S-band (12.6-cm wavelength) (9) (Fig. 1B) shows many regions of high backscatter cross section; other such regions extend beyond the limits of the map to latitudes as low as 67°N. The polarization characteristics of these regions are suggestive of cold-trapped volatiles (5, 6, 18). These radar-bright (RB) features generally coincide with high-latitude, steep-walled craters of which the southern floors are permanently shadowed from direct sunlight because of Mercury's near-zero obliquity. The largest RB features lie north of 85°N, whereas the 108-km-diameter Prokofiev crater [previously given the informal name "K" (18)] has a crescent-shaped

RB region behind its steep (17° slope) north-facing wall, just south of 85°N (Fig. 1B). With a depth-to-diameter ratio of 0.025, typical for a complex crater of this size, only a portion of its floor can lie in permanent shadow, consistent with the shape of the RB region. An unnamed 1.5-km-deep, 18-km-diameter crater "Z" lies on the central floor of Prokofiev and is RB. The 62-km-diameter crater Kandinsky (formerly "J") to the north has a nearly circular RB region (Fig. 1B). These and similar regions may now be subjected to illumination models that use detailed polar topography (19).

A plot of the maximum illumination flux over 10 solar days is shown in Fig. 1C. We modeled the primary shadowing of the finite disk of the Sun with the orbital and rotational geometry of Mercury following an earlier methodology (20). Zero flux corresponds to areas of near-permanent shadow that receive only scattered light. Mercury's orbital eccentricity and 3:2 spin-orbit resonance result in lower average solar flux near longitudes of 90° and 270°E. Shallow, degraded craters and craters lying near the 0° and 180°E longitudes of Mercury's equatorial "hot poles" have higher average illumination. Except for relatively fresh craters on the northern smooth plains (1), there are few RB features along these azimuths south of 85°N.

The reflectance measurements binned at 1 km by 1 km resolution are shown in Fig. 1D. The log-normally distributed quantity  $r_s$  has a mean of  $0.17 \pm 0.05$  (SD), and 98% of returns have  $r_s < 0.3$  (fig. S1). For comparison, the broadband geometric albedo of Mercury from space is 0.142 (21). About 7% of returns comprise a secondary "MLA-dark" (MD) mode distinguished by  $r_s < 0.1$ . This mode is seen in regions that are markedly darker than their surroundings. These regions coincide with areas where many received pulses do not trigger at the high threshold (fig. S2), although weak laser output, oblique incidence, steep terrain, and/or extreme range, as well as low reflectivity, can lead to poor signal recovery. The deficit of energy measurements in many MD regions indicates that the measured  $r_s$  values are upper bounds for surface albedoes that are lower by factors of 2 to 3 than their surroundings.

Many of the MD regions are associated with polar craters containing RB material (Fig. 2). The larger MD regions generally enclose the RB features. MD returns lie mainly within regions of very low peak illumination, although not necessarily permanent shadow. The reflectance is low

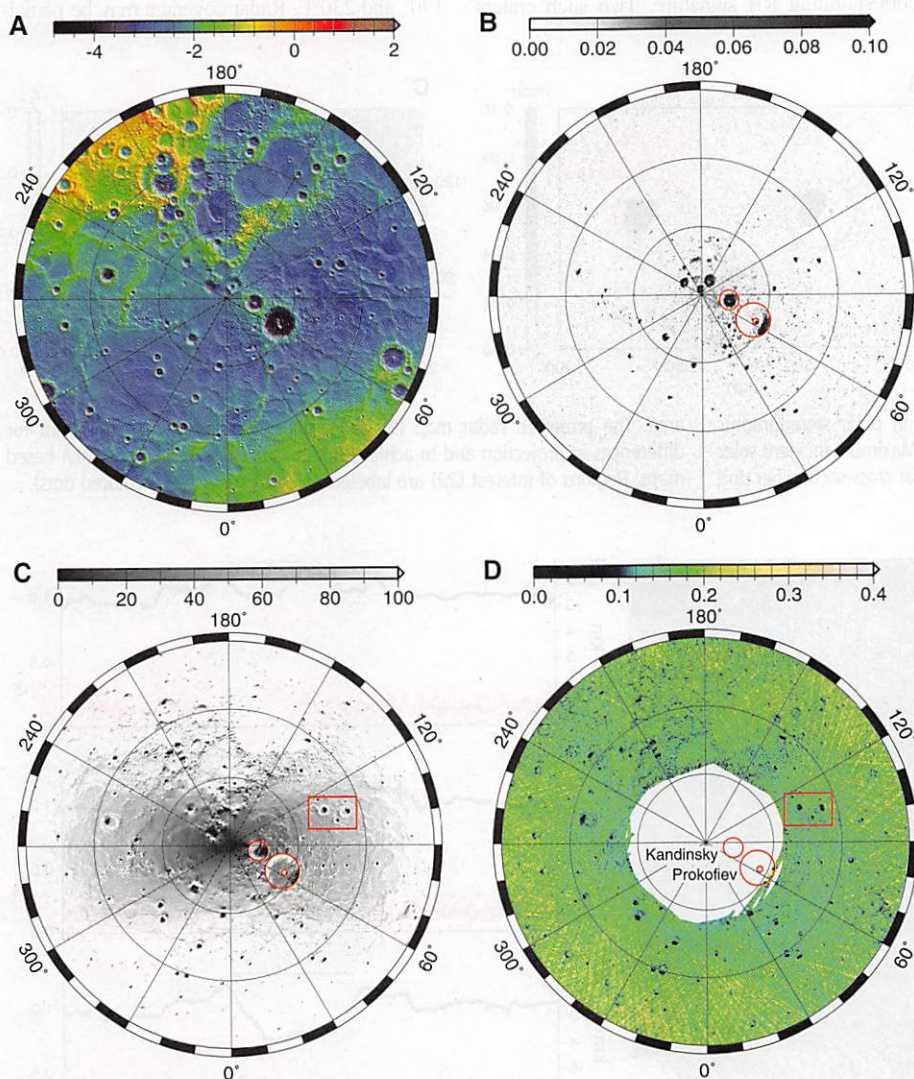


**Fig. 1.** Maps of topography, radar cross section, solar illumination, and reflectance in polar stereographic projection southward to 75°N. Kandinsky and Prokofiev craters are outlined in three of the four panels. (A) Topography (color scale in km) and shaded relief; the datum is a sphere of radius 2440 km. (B) Earth-based radar image (9) displayed as a dimensionless radar cross section per unit area. (C) Maximum incident solar flux over a 10-year period as a percentage of the solar constant at 1 astronomical unit (AU) from an illumination model. The red box outlines the region shown in Fig. 2. (D) The 1064-nm bidirectional reflectance from MLA low- and high-threshold measurements in near-nadir directions, median-averaged in 1 km-by-1 km bins. At latitudes poleward of 84°N, MLA obtained only a limited number of off-nadir profiles, and the projected reflectance data in this region are interpolated by a nearest-neighbor weighted average only within 2 km of data whose incidence angles were less than 10°.

**Table 1.** Classification of 175 craters according to radar and optical characteristics of associated deposits.

Radar	MLA dark	MLA bright/mixed	MLA normal	MLA undetermined
Bright	96	9	0	24
Dark	28	0	15	3

over the southern floors and the northward-facing walls of virtually all craters at latitudes between 75° and 84°N. Darkening also occurs on some poleward-facing exterior rim slopes of craters in the otherwise smooth plains within the 320-km-diameter Goethe basin. Such darkening extends into regions that are partially illuminated.

The asymmetric distribution of MD regions with respect to terrain slope direction does not simply result from observing geometry, surface roughness, or the magnitude of the surface slope. The pulses returning from the MD portions are not noticeably wider or narrower than those from the illuminated portions, nor do equator-facing portions of the floor show lower reflectance. If surface slope or roughness were causing reduced energy return, the darker regions would have a circu-

lar outline. The correspondence of dark material with pole-facing slopes and the lack of such darkening in most craters southward of 70°N appears to rule out instrumental effects or observational geometry as a cause of the surficial darkening.

To assess the relations between MLA-dark features, RB deposits, and illumination, we examined (22) 175 regions of low illumination identified as lying within craters varying in size from ~7 to 108 km in diameter (23) and from 65°N poleward (Table 1). All craters with RB deposits and sufficient MLA sampling show at least some MD features in their poleward-facing portions. Of 128 RB craters with RB deposits, 96 contain collocated MD portions, whereas there are 28 additional craters with MD material that lack a corresponding RB signature. Two such craters

(b5 and f5) (Fig. 2 and fig. S3) are relatively pristine (>1 km deep), so their interiors may not be visible to Earth-based radar. Twelve such craters are <14 km in diameter. Those craters with MD material that lack a RB signature and are 14 km or larger in diameter are at latitudes south of 80°N. As with the RB regions, MLA-dark deposits are more prevalent near 90° and 270°E, longitudes that receive less average illumination as a result of Mercury's spin-orbit resonance and eccentric orbit, and in fresh craters on the smooth plains. At latitudes north of 75°N, 15 similar shadowed regions (putatively small craters) with neither a RB signature nor MD material are located mainly on an elevated area surrounding Purcell crater between longitudes 170° and 230°E. Radar coverage may be partial-

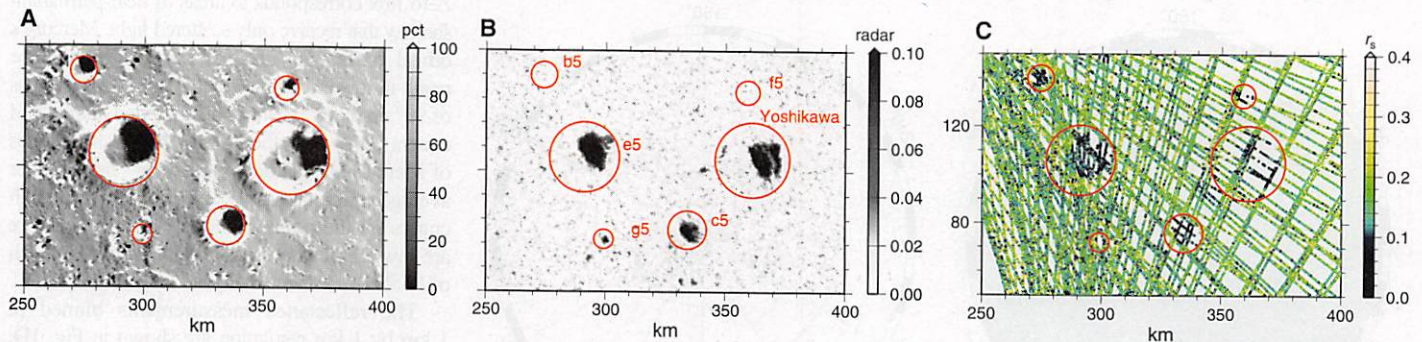


**Fig. 2.** Regional view of the area outlined in Fig. 1, in polar stereographic projection. Red circles show the outlines of six craters. (A) Maximum incident solar flux, as a percentage of the solar constant at 1 AU. (B) Radar cross-section per unit

area. The projected radar map (9) has been shifted by 4 km to account for differences in projection and to achieve optimal registration with the MLA-based maps. Regions of interest (22) are labeled. (C) MLA reflectance (colored dots).

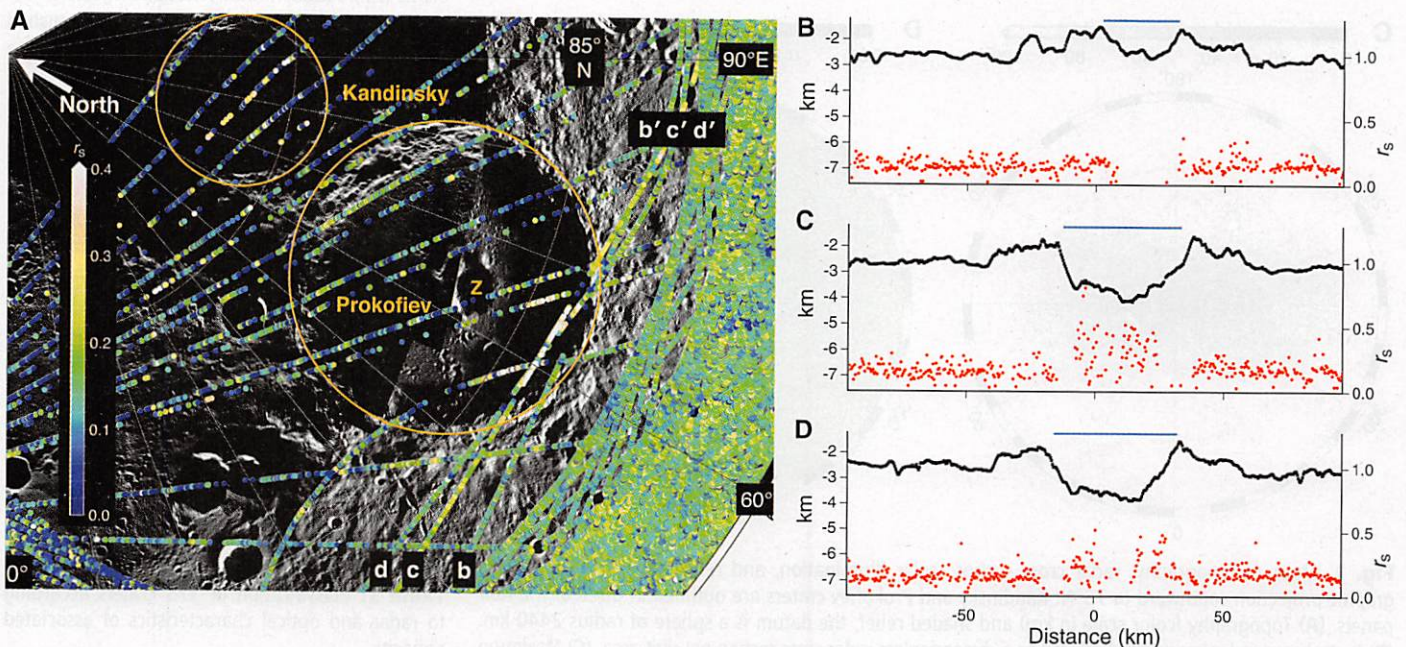


**Fig. 3.** (A) MLA reflectance measurements (colored dots) of the north polar region from longitude 0° to 90°E and latitude 82.5° to 90°N. Background is a mosaic of MDIS (34) frames at different illumination geometries and has a nonlinear contrast stretch for visibility. Three profiles through Prokofiev (b-b', c-c', and d-d') were acquired at near-nadir orientation. Profiles through Kandinsky were acquired at ~30° off-nadir orientation. (B to D) Profiles of

height (black lines) and reflectance (red dots) through Prokofiev acquired on 22 through 24 March 2012 starting at 0308 UTC on each day, at a 5° to 7° nadir angle. Vertical exaggeration is 10:1. The profiles are centered at longitude 60°E and traverse the poleward-facing wall of Prokofiev crater in an approximate west-to-east direction. The blue lines show the modeled extent of low average solar flux (<50 W m<sup>-2</sup> or <0.04 of terrestrial).

ly obscured by rough terrain in this sector, but the lack of RB features more likely has a thermal origin at these “hot pole” longitudes in locations where partial illumination might preclude stability of near-surface water ice (fig. S4).

Although the MLA-dark regions are more abundant and extensive than RB regions, there are at least nine areas within the largest RB regions at very high latitudes in which the MLA reflectances are optically bright. The nine craters hosting RB material, at latitudes between 82.5° and 88.5°N, have portions with  $r_s > 0.3$  as well as areas that are anomalously dark or that return no reflectance measurements. The two most prominent such craters are north of 84.9°N latitude.

Craters Kandinsky and Prokofiev, for which high radar cross sections suggest thick, near-surface ice deposits (18), are shown in Fig. 3. Their regions of permanent shadow (Fig. 1C) have many reflectance values in excess of 0.3 (pink or white symbols), especially along the southern portion of Prokofiev. Three profiles crossing the RB region are plotted along track in Fig. 3, B to D. Profile 3B grazed the uppermost kilometer of the crater wall and recorded no high-threshold detections in regions of shadow. Profile 3C passed 2 km into the interior along the north-facing wall and shows many strongly reflective returns (red symbols) up to the edges of the crater, where such returns dropped out for several seconds. Profile 3D reached portions of the crater floor that are in permanent shadow and recorded variable reflectance. These profiles are the only ones to date obtained over the shadowed interior of Prokofiev at the relatively small incidence angles (6° to 7°) for which reflectance measurements are most reliable. Two profiles nearest to crater Z (Fig. 3A) also include returns with  $r_s > 0.3$ , as do several traversing crater Kandinsky to the north, but the measurements are noisier owing to incidence angles greater than 25°.

The observations of 1064-nm reflectance from laser altimetry thus fall into three categories: Most are typical of Mercury reflectivity as a whole; a subset is much darker; and a smaller subset is substantially brighter. The association of MD regions with RB regions in near-permanent shadow suggests that a thin, radar-transparent layer of optically dark material overlies and surrounds the postulated polar ice deposits. If water ice were present in the ground as a matrix between mineral grains, it could lower the reflectance relative to dry ground but would sublimate rapidly and lose optical contrast if exposed to high temperatures. The presence of MD regions in many smaller craters without RB deposits, areas where scattered light raises average temperatures (2, 24), indicates the presence of volatiles that are both darker than water ice and stable to higher temperatures.

The identification of optically bright regions associated with large RB features at the highest (>84.9°N) latitudes is consistent with the hy-

pothesis that water ice is exposed at the surface in areas where surface temperatures are never sufficiently high for substantial loss by sublimation. The surface measurements are averages over footprints that are dozens of meters in extent and could represent a thin or unevenly distributed layer of optically bright material that has not been covered by dust or regolith. However, to the extent that MLA-bright and RB characteristics are sampling the same material, the associated deposits must have a thickness of at least several meters. The reflectance measurements presented here strongly suggest that one of the largest and deepest regions of permanent shadow in crater Prokofiev is a host for water ice deposits exposed at the surface.

The existence of these dark and bright surfaces and their association with topography indicates that their formation processes operated during geologically recent times and may be active on Mercury today. The rates of darkening and brightening must be higher than those for processes that act to homogenize surface reflectance, such as impact gardening. Were vertical mixing by impact gardening dominant at the meter scale, we would expect that the polar deposits would have reflectance values (and radar backscatter characteristics) more similar to those of surrounding terrain.

Detailed thermal models (25) suggest that surface temperatures in the majority of the high-latitude craters with RB deposits that MLA has observed to date are too warm to support persistent water ice at the surface, but the temperatures in their shadowed areas are compatible with the presence of surficial dark organic material. Modeled subsurface temperatures in these dark regions are permissive of stable water ice beneath a ~10-cm-thick layer of thermally insulating material. In contrast, thermal modeling of the bright areas is supportive of surface water ice. This interpretation of the surface reflectance at 1064 nm is fully consistent with the radar results as well as with neutron spectroscopic measurements of Mercury's polar regions (26). The bright and dark areas can be ascribed collectively to the deposition of water and organic volatiles derived from the impacts of comets or volatile-rich asteroids on Mercury's surface and migrated to polar cold traps via thermally stimulated random walk (27–29).

#### References and Notes

- M. T. Zuber *et al.*, *Science* **336**, 217 (2012).
- A. R. Vasavada, D. A. Paige, S. E. Wood, *Icarus* **141**, 179 (1999).
- K. Watson, B. C. Murray, H. Brown, *J. Geophys. Res.* **66**, 3033 (1961).
- J. R. Arnold, *J. Geophys. Res.* **84**, 5659 (1979).
- M. A. Slade, B. J. Butler, D. O. Muhleman, *Science* **258**, 635 (1992).
- J. K. Harmon, M. A. Slade, *Science* **258**, 640 (1992).
- B. J. Butler, D. O. Muhleman, M. A. Slade, *J. Geophys. Res.* **98**, 15,003 (1993).
- G. J. Black, D. B. Campbell, J. K. Harmon, *Icarus* **209**, 224 (2010).
- J. K. Harmon, M. A. Slade, M. S. Rice, *Icarus* **211**, 37 (2011).

- J. F. Cavanaugh *et al.*, *Space Sci. Rev.* **131**, 451 (2007).
- The MLA is a time-of-flight laser range finder that uses direct detection and pulse-edge timing to determine precisely the range from the MESSENGER spacecraft to Mercury's surface. MLA's laser transmitter emits 6-ns-long pulses at an 8-Hz rate with 20 mJ of energy at a wavelength of 1064 nm. Return echoes are collected by an array of four refractive telescopes and are detected with a single silicon avalanche photodiode detector. The timing of laser pulses is measured with a set of time-to-digital converters linked to a crystal oscillator for which the frequency is monitored from Earth.
- S. C. Solomon, R. L. McNutt Jr., R. E. Gold, D. L. Domingue, *Space Sci. Rev.* **131**, 3 (2007).
- M. J. Talpe *et al.*, *J. Geophys. Res.* **117**, E00113 (2012).
- G. B. Hansen, T. B. McCord, *J. Geophys. Res.* **109**, E01012 (2004).
- The MLA measures the threshold crossing times of the received pulses at two discriminator voltages simultaneously, a low threshold for maximum sensitivity and a threshold about twice as high to give four sample points of the received pulse waveform. A laser pulse may result in triggers at one or both thresholds or not at all. Ranging with low-threshold detections is possible at ranges up to 1500 km, but steady returns that cross both low and high thresholds are obtained mostly at altitudes less than ~600 km and with near-nadir (<20°) incidence. When a pulse is detected by a pair of discriminators, its energy and duration may be inferred from a model waveform that accounts for the dispersion in time of return pulses as a result of surface slope and/or roughness. To estimate the pulse energy, we adopted a simple triangular model that fits the rising and falling edges of the trigger at each threshold. This model generates values nearly equal to a Gaussian model for well-constrained pulses: Energy is a nonlinear function of pulse timing measurements and tends to have a long-tailed or approximate log-normal distribution, as illustrated in the supplementary materials.
- C. S. Gardner, *IEEE Trans. Geosci. Rem. Sens.* **30**, 1061 (1992).
- The lidar link equation is  $E_{rx} = E_{tx}\eta_r(A_r/R^2)(r_s/\pi)$ , where  $E_{rx}$  is the received signal pulse energy,  $E_{tx}$  is the transmitted laser pulse energy,  $\eta_r$  is the receiver optics transmission,  $A_r$  is the receiver telescope aperture area,  $R$  is range, and  $r_s$  is the target surface reflectivity (relative to Lambertian). The ratio  $r_s$  of reflected energy to incoming energy (i.e., irradiance/solar flux, often simply written  $I/F$ ) would be unity for a perfect diffusive reflector for which the transmitter and receiver orientation are perpendicular to the surface. Mercury's reflectivity at optical wavelengths normally lies in a range from 0.08 to 0.12 (30–32), but because of the opposition effect (33) the average 1064-nm reflectance is about 50% higher, or about 0.17.
- J. K. Harmon, P. J. Perillat, M. A. Slade, *Icarus* **149**, 1 (2001).
- The topography derived from 700 MLA profiles (29 March 2011 to 1 May 2012) provides a near-complete topographic map of the northern hemisphere northward to 84°N at a resolution of 0.5 km. Craters Prokofiev and Kandinsky were sampled by several off-nadir profiles, from which radial averages of topography were constructed and used to fill in the unsampled interior after adding pseudo-random noise, with a root variance of 70 m, and decimating and interpolating with the blockmedian and surface programs of the Generic Mapping Tools (<http://gmt.soest.hawaii.edu>). We modeled the average and maximum illumination conditions over a Mercury day by using an approach (20) developed to assess illumination conditions of polar regions of the Moon.
- E. Mazarico, G. A. Neumann, D. E. Smith, M. T. Zuber, M. H. Torrence, *Icarus* **211**, 1066 (2011).
- A. Mallama, D. Wang, R. A. Howard, *Icarus* **155**, 253 (2002).
- We selected 175 representative regions of interest from maps of permanent shadow derived from MLA topography, radar cross section, and MLA-dark regions, as shown in the supplementary materials. Because

many craters are not resolved by MLA, we also selected craters with diameters  $\geq 7$  km from MESSENGER images. Smaller RB deposits were not considered because most appear from images to lie in small secondary craters, at the foot of poleward-facing scarps, or in rough terrain and are inadequately sampled by MLA. The radar-bright deposits were mapped with a threshold of 0.075 in the MATLAB image processing toolbox and correlated with craters identified in MLA topography and MESSENGER images. Labels assigned in uppercase are consistent with previous nomenclature (15); lowercase letters and numerals were assigned to provisional features. Regions with MLA energy measurements were classified as dark, normal, or bright/mixed according to their contrast in brightness with those of surround areas; gaps in high-threshold returns were also taken to indicate darker material. Bright regions are surrounding those for which more than half of the returns have  $r_s > 0.3$ .

23. Diameters of large craters were fit to the maximum MLA topographic contours of the rims, whereas the diameters of smaller craters were estimated from Mercury Dual

Imaging System (34) image mosaics. Locations are less certain for smaller features inadequately sampled by MLA. Diameters of craters sampled ranged from 7 to 108 km, not including the 320-km-diameter Goethe basin. Not included are several degraded and partially flooded craters, such as a 133-km-diameter degraded crater that encloses Purcell but for which the relief does not create an area of permanent shadow.

24. D. A. Paige, S. E. Wood, A. R. Vasavada, *Science* **258**, 643 (1992).
25. D. A. Paige *et al.*, *Science* **339**, 300 (2013); 10.1126/science.1231106.
26. D. J. Lawrence *et al.*, *Science* **339**, 292 (2013); 10.1126/science.1229953.
27. B. J. Butler, *J. Geophys. Res.* **102**, 19,283 (1997).
28. J. A. Zhang, D. A. Paige, *Geophys. Res. Lett.* **36**, L16203 (2009).
29. J. A. Zhang, D. A. Paige, *Geophys. Res. Lett.* **37**, L03203 (2010).
30. T. B. McCord, J. B. Adams, *Science* **178**, 745 (1972).
31. F. Vilas, *Icarus* **64**, 133 (1985).

32. W. E. McClintock *et al.*, *Science* **321**, 62 (2008).
33. T. Gehrels, *Astrophys. J.* **123**, 331 (1956).
34. S. E. Hawkins III *et al.*, *Space Sci. Rev.* **131**, 247 (2007).

**Acknowledgments:** The MESSENGER project is supported by the NASA Discovery Program under contracts NAS5-97271 to the Johns Hopkins University Applied Physics Laboratory and NASW-00002 to the Carnegie Institution of Washington. We are grateful for the myriad of contributions from the MLA instrument and MESSENGER spacecraft teams and for comments by P. Lucey and two anonymous referees that improved the manuscript.

**Supplementary Materials**  
[www.sciencemag.org/cgi/content/full/science.1229764/DC1](http://www.sciencemag.org/cgi/content/full/science.1229764/DC1)  
 Supplementary Text  
 Figs. S1 to S5  
 Reference (35)

5 September 2012; accepted 14 November 2012  
 Published online 29 November 2012;  
 10.1126/science.1229764

# Thermal Stability of Volatiles in the North Polar Region of Mercury

David A. Paige,<sup>1\*</sup> Matthew A. Siegler,<sup>1,2</sup> John K. Harmon,<sup>3</sup> Gregory A. Neumann,<sup>4</sup> Erwan M. Mazarico,<sup>4</sup> David E. Smith,<sup>5</sup> Maria T. Zuber,<sup>5</sup> Ellen Harju,<sup>1</sup> Mona L. Delitsky,<sup>6</sup> Sean C. Solomon<sup>7,8</sup>

Thermal models for the north polar region of Mercury, calculated from topographic measurements made by the MErcury Surface, Space ENvironment, GEochemistry, and Ranging (MESSENGER) spacecraft, show that the spatial distribution of regions of high radar backscatter is well matched by the predicted distribution of thermally stable water ice. MESSENGER measurements of near-infrared surface reflectance indicate bright surfaces in the coldest areas where water ice is predicted to be stable at the surface, and dark surfaces within and surrounding warmer areas where water ice is predicted to be stable only in the near subsurface. We propose that the dark surface layer is a sublimation lag deposit that may be rich in impact-derived organic material.

Earth-based radar observations have yielded maps of anomalously bright, depolarizing features on Mercury that appear to be localized in permanently shadowed regions near the planet's poles (1, 2). Observations of similar radar signatures over a range of radar wavelengths imply that the radar-bright features correspond to deposits that are highly transparent at radar wavelengths and extend to depths of several meters below the surface (3). Cold-trapped water ice has been proposed as the most likely material to be responsible for these features (2, 4, 5), but other volatile species that are abundant on Mercury, such as sulfur, have also been suggested (6).

Measurements of surface reflectance at a wavelength of 1064 nm, made with the Mercury Laser Altimeter (MLA) onboard the MESSENGER (MErcury Surface, Space ENvironment, GEochemistry, and Ranging) spacecraft, have revealed the presence of surface material that collocates approximately with radar-bright areas within north polar craters and that has approximately half the average reflectance of the planet, as well as bright material within Kandinsky and Prokofiev craters that has approximately twice the average planetary reflectance (7). MLA measurements have also provided detailed maps of the topography of Mercury's north polar region (8). Here, we apply this information in conjunction with a ray-tracing thermal model, previously used to predict temperatures in the polar regions of Earth's Moon (9), to calculate the thermal stability of volatile species in the north polar region of Mercury.

Maximum and average modeled temperatures (10) over one complete 2-year illumination cycle for the north polar region of Mercury are shown in Fig. 1, A and B. The topography model north of 84°N latitude has been extrapolated from only a few off-nadir data tracks, so model temperatures within this circle should be taken only as

estimates. On Mercury, biannual average temperatures can be interpreted as close approximations to the nearly constant subsurface temperatures that exist below the penetration depths of the diurnal temperature wave [about 0.3 to 0.5 m for ice-free regolith, and several meters for ice-rich areas (5, 9)]. The latitudinal and longitudinal symmetries in surface and near-surface temperatures result from Mercury's near-zero obliquity, eccentric orbit, and 3:2 spin-orbit resonance (11, 12).

Comparison between the areal coverage of model-calculated biannual maximum and average temperatures and the thermal stability of a range of candidate volatile species (Fig. 2) provides strong evidence that Mercury's anomalous radar features are due dominantly to the presence of thermally stable water ice, rather than some other candidate frozen volatile species. Within the region sampled, the vast majority of locations within which biannual average temperatures are less than ~100 K are radar-bright, whereas for areas with biannual average temperatures of greater than 100 K there are almost no radar-bright deposits (Fig. 2C). This distribution suggests that the radar-bright features are due to the presence of a volatile species that is not thermally stable at temperatures higher than ~100 K. Because of the exponential dependence of vacuum sublimation loss rates with temperature, the thermal stabilities of the candidate volatile species shown in Fig. 2A over time scales of millions to billions of years are well separated in temperature. As shown in Fig. 2A and fig. S8, 1 mm of exposed water ice—or 1 mm of water ice buried beneath a 10-cm-thick lag deposit—would sublimate to a vacuum in 1 billion years at temperatures of 100 to 115 K, which we interpret as strong evidence that Mercury's anomalous radar features are due dominantly to the presence of thermally stable water ice. If the radar-bright deposits were composed primarily of a material with a higher or lower volatility than water ice, we would expect them to be thermally stable in areas with lower or higher annual average temperatures than we observe. As illustrated in Fig. 2, B and C, the fractional areal coverage of radar-bright regions that are also just sufficiently

<sup>1</sup>Department of Earth and Space Sciences, University of California, Los Angeles, CA 90095, USA. <sup>2</sup>Jet Propulsion Laboratory, Pasadena, CA 91109, USA. <sup>3</sup>National Astronomy and Ionosphere Center, Arecibo, PR 00612, USA. <sup>4</sup>NASA Goddard Space Flight Center, Greenbelt, MD 20771, USA. <sup>5</sup>Department of Earth, Atmospheric and Planetary Sciences, Massachusetts Institute of Technology, Cambridge, MA 02139, USA. <sup>6</sup>California Specialty Engineering, Flintridge, CA 91012, USA. <sup>7</sup>Department of Terrestrial Magnetism, Carnegie Institution of Washington, Washington, DC 20015, USA. <sup>8</sup>Lamont-Doherty Earth Observatory, Columbia University, Palisades, NY 10964, USA.

\*To whom correspondence should be addressed. E-mail: dap@moon.ucla.edu

cold to trap subsurface water is nearly unity, whereas for elemental sulfur, the fractional area is less than 1 in 500. Although the temperatures of Mercury's radar-bright regions are not a good match to thermal stability temperatures of sulfur, the existence of cold traps at lower latitudes dominated by sulfur and other less volatile cold-trapped species cannot be excluded, nor can the possibility that Mercury's water-ice cold traps themselves also contain minor quantities of less volatile cold-trapped species.

The calculated depths at which near-surface water ice would be lost to sublimation at a rate of less than 1 mm per billion years, under the assumption that the ice deposits are covered by material that has the same thermophysical properties as average surface material on Mercury (5, 10), are shown in Fig. 1C. The thermal model results predict that most of Mercury's water ice deposits equatorward of 83°N would be thermally stable only if buried beneath a ~10-cm-thick layer of low-conductivity, ice-free, soil-like material—a result consistent with interpretations of available radar data (3). At higher latitudes, the thermal model results predict that temperatures in larger impact craters are sufficiently cold to permit the stability of surface ice deposits. The observation of anomalously high MLA surface reflectance values in Kandinsky and Prokofiev craters (7) is consistent with the interpretation that the polar deposits in those craters contain water ice exposed at the surface.

Comparisons of the areal coverage of model-calculated biannual maximum and average temperatures for MLA-dark areas to all areas measured by MLA in the circumpolar region 75° to 83°N are shown in Fig. 2, D and E. The MLA-dark regions display a wider range of temperatures and are spatially more extensive than the radar-bright regions, even after accounting for Earth visibility.

Area ratios for biannual maximum temperatures in MLA-dark regions peak near 0.8 at ~160 K and decrease rapidly at progressively lower temperatures. We interpret this trend as indicating an increasing tendency for the thermal stability of bright surface water ice deposits as biannual maximum temperatures approach 100 K, which we document in an unusually cold impact crater at 82.0°N, 215°E (fig. S3).

In total, the results of the thermal model calculations combined with radar and MLA reflectance measurements present a quantitatively consistent case that Mercury's polar deposits are composed dominantly of water ice. This conclusion is independently reinforced by measurements of the flux of fast and epithermal neutrons made with MESSENGER's Neutron Spectrometer (13). In the region studied, radar-bright deposits are observed to be in essentially every surface and subsurface location where water ice is thermally

stable.

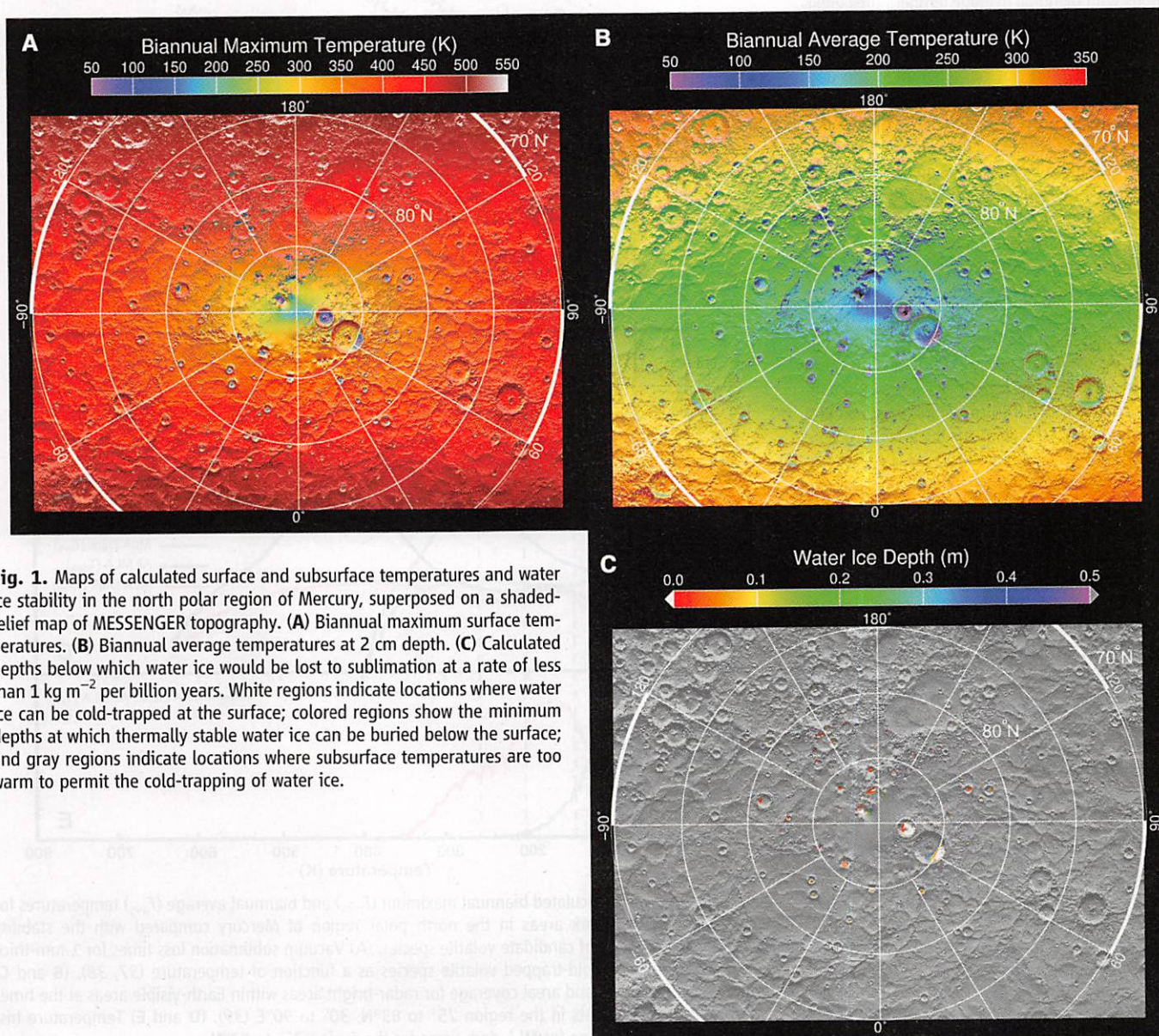


**Fig. 1.** Maps of calculated surface and subsurface temperatures and water ice stability in the north polar region of Mercury, superposed on a shaded-relief map of MESSENGER topography. (A) Biannual maximum surface temperatures. (B) Biannual average temperatures at 2 cm depth. (C) Calculated depths below which water ice would be lost to sublimation at a rate of less than  $1 \text{ kg m}^{-2}$  per billion years. White regions indicate locations where water ice can be cold-trapped at the surface; colored regions show the minimum depths at which thermally stable water ice can be buried below the surface; and gray regions indicate locations where subsurface temperatures are too warm to permit the cold-trapping of water ice.

stable, despite the activity of such ice destruction processes as Lyman  $\alpha$  photodissociation (14) and burial by meteoroid gardening (15). Calculated temperatures in the coldest locations on Mercury are sufficiently low that water molecules in these cold traps have very little diffusive mobility (16). The fact that bright surface ice deposits are observed in these locations requires a geologically recent or ongoing supply of water. In regions of currently stable ground ice, temperatures are sufficiently warm to allow for diffusive vertical and lateral mobility of water (17), which has enabled water to actively migrate to sites of present thermal stability.

The thermal model results provide insights into the nature and origin of MLA-dark surface deposits. Figure 2D shows that equatorward of 84°N dark material is found almost universally in regions with biannual average temperatures of 100 K and biannual maximum temperatures of 160 K, but dark material is entirely absent in regions with biannual average temperatures greater than 210 K and biannual maximum temperatures greater than 300 K. This systematic temperature dependence would not be apparent if the dark material were being redistributed about this region by impact processes alone. The distribution of dark material must be controlled by the presence of volatile substances that are not thermally stable above these temperatures. Given the clear association between the dark material and water ice that exists on Mercury today, we suggest that one of these volatile substances is water. As shown in Fig. 2A and fig. S7, the temperature at which a water ice deposit can be considered thermally stable depends on the time scale under consideration. At a temperature of 102 K, for instance, a meter-thick layer of pure water ice would sublimate to space in 1 billion years, whereas at a temperature of 210 K, a meter-thick layer of pure water ice would sublimate in 35 days.

We suggest that the MLA-dark deposits are largely sublimation lags formed on the surfaces of metastable water ice—that is, that Mercury's polar deposits were more extensive at some point in the past, and then retreated rapidly to their present long-term thermally stable state. Because Mercury's low obliquity [ $2.04 \pm 0.08$  arc min (18)] is likely to have persisted since its capture into a Cassini state >3.5 billion years ago (19), thermal conditions at Mercury's poles have been relatively stable. The formation of the MLA-dark deposits by sublimation lag requires episodic, but temporally coincident, sources of both water and nonwater contaminants. Because metastable ice deposits must accumulate on time scales that are shorter than those at which they sublimate, the formation of the MLA-dark deposits by sublimation lag is compatible with episodic deposition of water and other volatiles by asteroids and comets.

The composition of the MLA-dark deposits is not known. However, materials with similarly low albedos are routinely observed on the surfaces of comets (20, 21), asteroids (22–24), and outer solar system objects (25, 26) and are generally

attributed to the presence of macromolecular carbonaceous material, rather than to the effects of radiation damage of pure ice (22, 24–26). As shown in Fig. 2, the thermal stability temperatures of a selection of simple organic compounds are such that if they were present in the Mercury polar environment, they would be readily incorporated into accumulating water ice deposits and cold-trapped directly onto surrounding warmer regions. The processing of simple organic material into dark macromolecular carbonaceous material is facilitated by high-energy photons and particles (10, 27–31), which are abundant in Mercury's polar environment because of the configuration of magnetic field lines and the pattern of ion precipitation at Mercury's high latitudes (10, 32, 33). Under this scenario, asteroidal and cometary impacts episodically release water and simple organic compounds into the Mercury en-

vironment, where they migrate to the polar regions, become cold-trapped, and accumulate. The mixture of water ice and organic material sublimates and is reprocessed to form a dark sublimation lag deposit that is analogous to that observed on the surfaces of comet nuclei today. The radar absorption properties of low-density macromolecular carbonaceous material have been measured and are found to be less lossy than low-density soil (34). Therefore, the presence of a layer of organic-rich material overlying ground ice deposits, or the presence of minor concentrations of organic-rich material within ice deposits, is not inconsistent with available radar observations. The possibility for synthesis of organic compounds in the permanently shadowed regions of Earth's Moon has been suggested (35), and the spectroscopic detection of simple organic compounds during the impact of the Lunar Crater

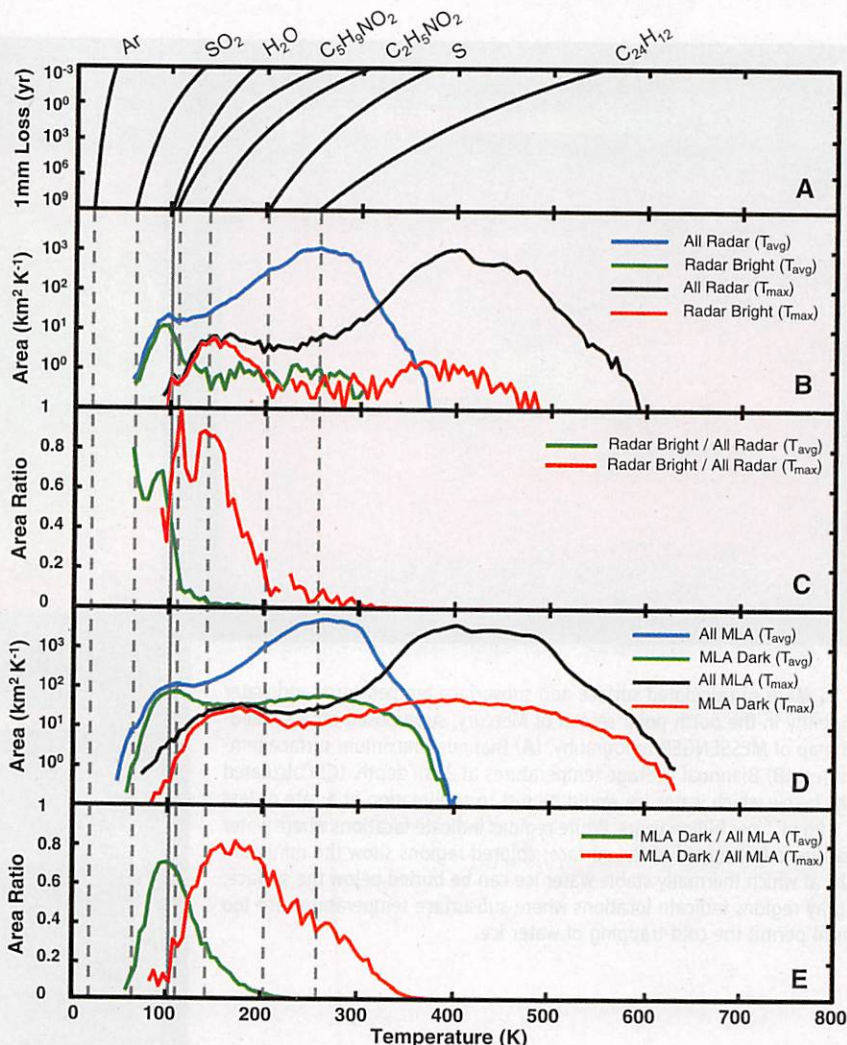


**Fig. 2.** Histograms of calculated biannual maximum ( $T_{\max}$ ) and biannual average ( $T_{\text{avg}}$ ) temperatures for radar-bright and MLA-dark areas in the north polar region of Mercury compared with the stability temperatures of a range of candidate volatile species. (A) Vacuum sublimation loss times for 1-mm-thick pure layers of selected cold-trapped volatile species as a function of temperature (37, 38). (B and C) Temperature histograms and areal coverage for radar-bright areas within Earth-visible areas at the times of the radar measurements in the region 75° to 83°N, 30° to 90°E (39). (D and E) Temperature histograms and areal coverage for MLA-dark areas for the region 75° to 83°N.

Observation and Sensing Satellite (36) provides further evidence that organic material and organic precursors coexist within the polar cold traps of solar system airless bodies.

Forming Mercury's ground ice deposits via the sublimation of a mixture of water ice and organic contaminants solves a long-standing problem regarding their origin. Today, thick deposits of ground ice are found near 75°N in areas with biannual maximum surface temperatures in excess of 150 K. At these temperatures, pure exposed water ice deposited by a cometary impact would sublimate at a rate of 1 m per 1000 years. The ice deposit would disappear on time scales of tens of thousands of years if not thermally protected by a ~10-cm-thick layer of overlying ice-free material, but this geometry is problematic because the time scales for burial to these depths by impact-gardened soil from adjacent regions is estimated to be on the order of tens of millions of years (3, 15). If Mercury's ground ice deposits contain sufficient less-volatile cold-trapped contaminants to create a surface lag deposit as they sublimate, then it would not be necessary to invoke a recent cometary impact to explain their present vertical and horizontal distribution. The fact that all of Mercury's surface and subsurface water ice deposits appear to be in a thermally stable configuration means that the sources of water and the mobility of water in Mercury's environment are sufficiently robust to overcome the combined effects of all other processes that would tend to destroy and disrupt them.

#### References and Notes

- M. A. Slade, B. J. Butler, D. O. Muhleman, *Science* **258**, 635 (1992).
- J. K. Harmon, M. A. Slade, M. S. Rice, *Icarus* **211**, 37 (2011).

- J. K. Harmon, *Space Sci. Rev.* **132**, 307 (2007).
- D. A. Paige, S. E. Wood, A. R. Vasavada, *Science* **258**, 643 (1992).
- A. R. Vasavada, D. A. Paige, S. E. Wood, *Icarus* **141**, 179 (1999).
- A. L. Sprague, D. M. Hunten, K. Lodders, *Icarus* **118**, 211 (1995).
- G. A. Neumann *et al.*, *Science* **339**, 296 (2013); 10.1126/science.1229764.
- M. T. Zuber *et al.*, *Science* **336**, 217 (2012).
- D. A. Paige *et al.*, *Science* **330**, 479 (2010).
- See supplementary materials on Science Online.
- S. Soter, J. Ulrichs, *Nature* **214**, 1315 (1967).
- Despite the extreme range of surface temperatures on Mercury, Fig. 1B indicates that there exists a ~4°-wide circumpolar zone with annual average temperatures between 273 and 373 K, a potential near-surface environment for liquid water that is the most extensive in the solar system outside Earth.
- D. J. Lawrence *et al.*, *Science* **339**, 292 (2013); 10.1126/science.1229953.
- T. H. Morgan, D. E. Shemansky, *J. Geophys. Res.* **96**, 1351 (1991).
- D. Crider, R. M. Killen, *Geophys. Res. Lett.* **32**, L12201 (2005).
- N. Schorghofer, G. J. Taylor, *J. Geophys. Res.* **112**, E02010 (2007).
- M. A. Siegler, B. G. Bills, D. A. Paige, *J. Geophys. Res.* **116**, E03010 (2011).
- J. L. Margot *et al.*, *J. Geophys. Res.* **117**, E00109 (2012).
- S. J. Peale, *Astrophys. J.* **79**, 722 (1974).
- R. Z. Sagdeev *et al.*, *Nature* **321**, 262 (1986).
- H. U. Keller, L. Jorda, in *The Century of Space Science*, J. A. M. Bleeker, J. Geiss, M. Huber, Eds. (Kluwer Academic, Dordrecht, Netherlands, 2001), vol. 2, pp. 1235–1276.
- J. Gradie, J. Veverka, *Nature* **283**, 840 (1980).
- E. F. Tedesco *et al.*, *Astron. J.* **97**, 580 (1989).
- J. F. Bell, D. R. Davis, W. K. Hartmann, M. J. Gaffey, in *Asteroids II*, R. P. Binzel, T. Gehrels, M. S. Matthews, Eds. (Univ. of Arizona Press, Tucson, AZ, 1989), pp. 921–945.
- D. P. Cruikshank, C. M. Dalle Ore, *Earth Moon Planets* **92**, 315 (2003).

- D. P. Cruikshank, T. L. Roush, M. J. Bartholomew, T. R. Geballe, Y. J. Pendleton, *Icarus* **135**, 389 (1998).
- D. L. Mitchell *et al.*, *Icarus* **98**, 125 (1992).
- R. E. Johnson, J. F. Cooper, L. J. Lanzerotti, G. Strazzulla, *Astron. Astrophys.* **187**, 889 (1987).
- L. J. Lanzerotti *et al.*, *J. Geophys. Res.* **92**, 14949 (1987).
- R. E. Johnson, *J. Geophys. Res.* **96**, 17553 (1991).
- R. E. Johnson, in *Solid-State Astrophysics, Enrico Fermi Series*, G. Strazzulla, E. Bussoletti, Eds. (North Holland, Amsterdam, 1991), pp. 129–168.
- J. A. Slavin *et al.*, *Science* **324**, 606 (2009).
- N. Mouawad *et al.*, *Icarus* **211**, 21 (2011).
- P. Paillou *et al.*, *Geophys. Res. Lett.* **35**, L18202 (2008).
- P. G. Lucey, *Proc. SPIE* **4137**, 84 (2000).
- A. Colaprete *et al.*, *Science* **330**, 463 (2010).
- J. A. Zhang, D. A. Paige, *Geophys. Res. Lett.* **36**, L16203 (2009).
- J. A. Zhang, D. A. Paige, *Geophys. Res. Lett.* **37**, L03203 (2010).
- This region was selected because it has the highest density of Earth-based radar measurements at the most favorable viewing geometries.

**Acknowledgments:** Supported by NASA grant NNX07AR64G. We thank L. Carter, A. McEwen, D. Schriver, and M. Slade for assistance with this research. The MESSENGER project is supported by the NASA Discovery Program under contract NASS-97271 to The Johns Hopkins University Applied Physics Laboratory and NASW-00002 to the Carnegie Institution of Washington. MESSENGER data used in this study are available through the NASA Planetary Data System Geosciences Node. Arecibo radar data used in this study are available at [www.naic.edu/~radarus1/Mercpole](http://www.naic.edu/~radarus1/Mercpole).

#### Supplementary Materials

[www.sciencemag.org/cgi/content/full/science.1231106/DC1](http://www.sciencemag.org/cgi/content/full/science.1231106/DC1)  
Materials and Methods  
Figs. S1 to S8  
References (40–56)

4 October 2012; accepted 14 November 2012  
Published online 29 November 2012;  
10.1126/science.1231106

## An Efficient Polymer Molecular Sieve for Membrane Gas Separations

Mariolino Carta,<sup>1</sup> Richard Malpass-Evans,<sup>1</sup> Matthew Croad,<sup>1</sup> Yulia Rogan,<sup>1</sup> Johannes C. Jansen,<sup>2</sup> Paola Bernardo,<sup>2</sup> Fabio Bazzarelli,<sup>2</sup> Neil B. McKeown<sup>1\*</sup>

Microporous polymers of extreme rigidity are required for gas-separation membranes that combine high permeability with selectivity. We report a shape-persistent ladder polymer consisting of benzene rings fused together by inflexible bridged bicyclic units. The polymer's contorted shape ensures both microporosity—with an internal surface area greater than 1000 square meters per gram—and solubility so that it is readily cast from solution into robust films. These films demonstrate exceptional performance as molecular sieves with high gas permeabilities and good selectivities for smaller gas molecules, such as hydrogen and oxygen, over larger molecules, such as nitrogen and methane. Hence, this polymer has excellent potential for making membranes suitable for large-scale gas separations of commercial and environmental relevance.

Commercially important membrane-based gas separations include O<sub>2</sub> and N<sub>2</sub> enrichment of air, hydrogen recovery from ammonia production or hydrocarbon processing, and the upgrading of natural gas (1). They also have potential for both post-combustion and pre-combustion CO<sub>2</sub> capture during electricity generation from fossil fuels (2, 3). Polymer mem-

branes provide an energy-efficient method for gas separations because they do not require thermal regeneration, a phase change, or active moving parts in their operation and as such are predicted to play a growing role in an energy-constrained and low-carbon future (4). However, polymers suffer from a well-defined trade-off between the desirable properties of permeability and selec-

tivity for the required gas component. Presently, most commercial gas-separation membranes are based on a few polymers with low permeability and high selectivity; therefore, large membrane areas are required to compensate for lack of permeance, which increases costs and space requirements for large-scale applications. Unfortunately, highly permeable microporous polymers demonstrate insufficient selectivity for practical applications because, unlike classical molecular sieves such as zeolites, they possess ill-defined voids that because of chain flexibility fluctuate in size and so have limited size-selectivity (5). However, microporous polymers have the great advantage over classical inorganic molecular sieve materials of being easily processed into membranes (such as thin coatings or hollow fibers). Therefore, it is an important challenge to develop microporous polymers that behave as efficient

<sup>1</sup>School of Chemistry, Cardiff University, Cardiff CF10 3AT, UK.

<sup>2</sup>Institute on Membrane Technology, Consiglio Nazionale delle Ricerche, ITM-CNR, c/o University of Calabria, Via P. Bucci 17/C, 87030 Rende (CS), Italy.

\*To whom correspondence should be addressed. E-mail: [mckeownnb@cardiff.ac.uk](mailto:mckeownnb@cardiff.ac.uk).

molecular sieves so that they can provide both the permeability and selectivity to support large-scale gas separations.

Robeson used data from a very large number of polymers to quantify the trade-off between single gas permeability ( $P_x$ ) and ideal selectivity ( $\alpha_{xy} = P_x/P_y$ ) for a number of gas pairs (6, 7). Empirical upper bounds in plots of  $\log \alpha_{xy}$  versus  $\log P_x$  were established, and the position of data points of new polymers relative to these upper bounds is used routinely as an indicator of their potential performance for gas separations. In effect, the positions of the upper bounds represent the state of the art for approaching true molecular sieve behavior in polymers. Hence, rigid glassy polymers that facilitate size-selective gas diffusivity through reduced chain mobility, especially those composed of fused-ring ladder-like structures such as polymers of intrinsic microporosity (PIMs; PIM-1, for example) (Fig. 1C), help to define the present upper bounds (6, 8). Freeman's theoretical analysis of the position of the upper bounds suggests that further enhancement in gas selectivities could be achieved by designing polymers with even greater shape persistence (9). Recently, we tested this prediction by making a PIM in which the relatively flexible spirobisindane (SBI) component of PIM-1

was replaced with the more rigid spirobifluorene unit (PIM-SBF). The enhanced gas selectivities demonstrated by PIM-SBF resulted in data with modest advances above the current Robeson upper bounds for most gas pairs of interest (10). However, because of the inherent flexibility of the spiro-centers and dioxan linking groups used to assemble these PIMs (11), a fundamental structural redesign is required to provide microporous polymers that offer substantial further increases in rigidity and performance.

Molecular modeling of potential structural components for assembling polymers with greater shape-persistence suggests that bridged bicyclic ring systems, such as ethanoanthracene (EA), are highly inflexible when compared with the spiro-centers and dioxan rings used commonly within PIMs (Fig. 1D). However, devising an efficient polymerization reaction on the basis of forming bridged bicyclic linking groups is a difficult synthetic challenge because of the need for the simultaneous formation of multiple covalent bonds. With this challenge in mind, we noted that the bridged bicyclic amine 2,8-dimethyl-6H,12H-5,11-methanodibenzo[b,f][1,5]diazocine, commonly called Tröger's base (TB), can be prepared in excellent yield, despite requiring the participation of five precursor molecules and the net

formation of six covalent bonds for its construction (12). TB was originally reported in 1887 after its serendipitous isolation from the reaction between *p*-toluidine and dimethoxymethane (13) and has since been the subject of numerous studies because of its interesting stereochemistry (14), supramolecular chemistry (15, 16), and strongly basic nature for organocatalysis (17). However, TB has rarely been used as a component for polymer construction (18, 19), and these previous studies involved preformed TB monomers rather than in situ formation of the TB unit during the polymerization reaction. The rigidity conferred on TB by its bridged bicyclic structure was confirmed through modeling (Fig. 1D); therefore, it was anticipated that polymers prepared by using TB polymerization from suitably rigid aromatic diamine monomers would be highly shape-persistent. Hence, we designed two monomers, 2,6(7)-diamino-9,10-dimethylethanoanthracene and 5,5',6,(6'),1'-diamino-3,3,3',3'-tetramethyl-1,1'-spirobisindane, to assess the efficiency of the proposed TB polymerization reaction and, if successful, to provide PIM-like fused-ring macromolecular structures.

Once synthesized, each monomer was subsequently reacted with five equivalents of dimethoxymethane in trifluoroacetic acid (TFA) at

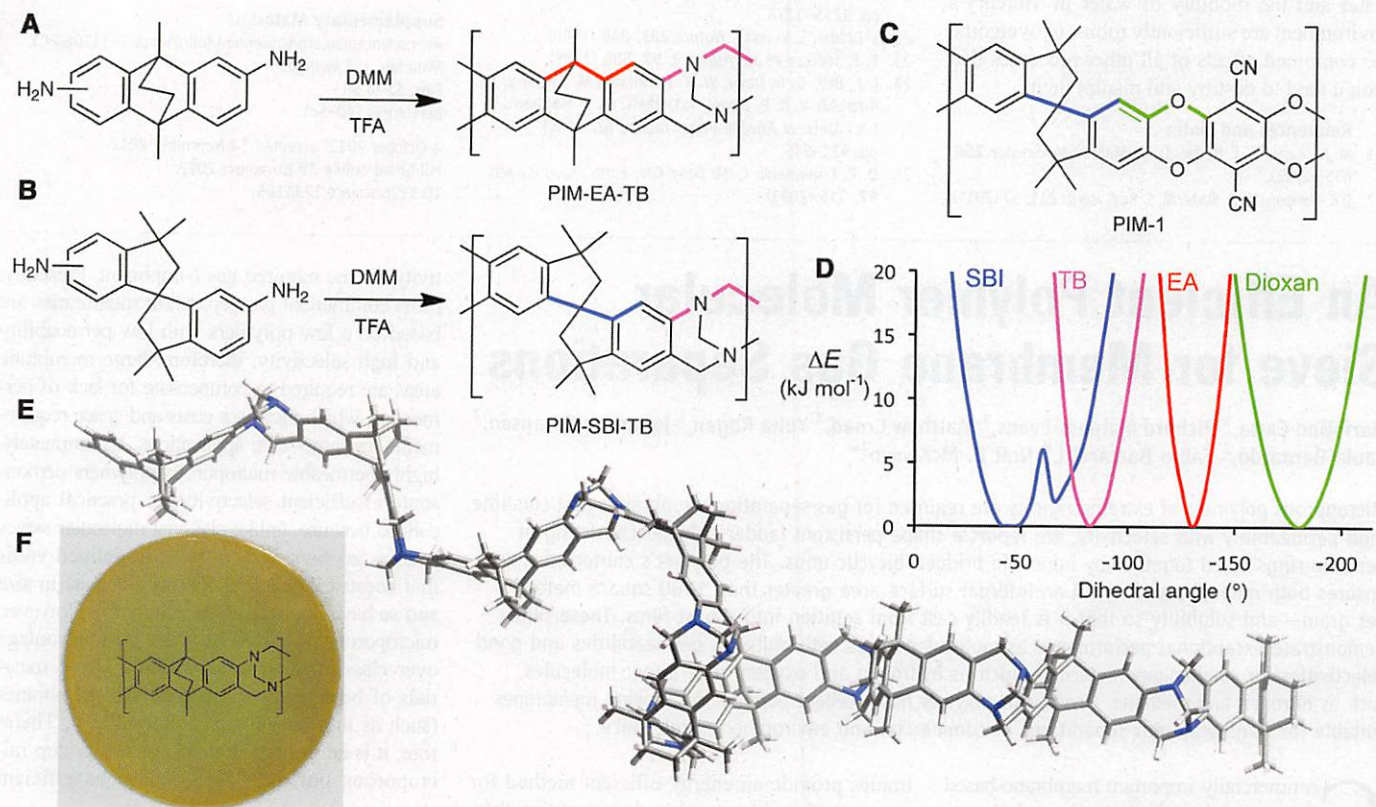


**Fig. 1.** The synthesis and molecular structures of (A) PIM-EA-TB and (B) PIM-SBI-TB (DMM, dimethoxymethane; TFA, trifluoroacetic acid). (C) The structure of PIM-1, the archetypal PIM. (D) A plot showing the increase in energy associated with the deviation in the marked dihedral angle within the bridged bicyclic units of EA (red) and TB (purple) as compared with typical components of PIMs, such as the spiro-center of SBI (blue) and the dioxan linking unit

(green). The narrower energy wells of the bridged bicyclic units TB and EA demonstrate their greater rigidity. (E) A molecular model of PIM-EA-TB showing its contorted shape, which combined with its rigidity generates intrinsic microporosity due to an inability to pack efficiently in the solid state. (F) A solvent-cast film (10 cm in diameter) of PIM-EA-TB, through which is visible its molecular structure printed on a piece of paper.